Network-based analysis of seismo-volcanic tremors

Nikolai M. Shapiro
Jean Soubestre
Cyril Journeau

June 20, 2023

Abstract

Volcanic tremors represent one of the most important class of seismo-volcanic signals due to their abundant presence in seismic records, their wealth of information regarding magmatic systems, their use as a tool for monitoring the state of volcanoes and their potential as precursor signals to eruptions. These signals have been analyzed for several decades with single station approaches, from which empirical inferences can be made regarding their sources, generation mechanism and scaling relations with eruptions parameters. Modernisation and densification of instrumentation networks coupled with sophistication of analysis methods and enhanced computation capacities, allow to switch from single-station to full seismic network based methods. We introduce in this chapter the inter-station cross-correlations methods, the estimation of the network covariance matrix and the study of its eigenvalues and eigenvectors. Such advanced methods enable to measure temporal, spatial and spectral tremor properties. They are contained in the CovSeisNet Python package which has been used for characterizing various tremor episodes, including two examples from Kilauea volcano, Hawaii and Klyuchevskoy Volcanic Group, Kamchatka presented in this chapter. These application examples illustrate the complexity of tremors and emphasize the need to continue the development of new algorithms aimed at the exploration of network covariances to better constrain the different tremor generation processes that can be multiple, simultaneous and interacting. In particular, the combination of network-based analysis with polarization and machine learning approaches may represent a new step in our understanding of the underlying phenomena. In turn, this enhanced discernment of the involved processes and the links with the properties of the volcanic system can lead to a more effective monitoring and ultimately a better apprehension of volcanic system destabilizations and anticipation of the associated unrests.

Contents

1 Introduction

Active geological and environmental processes produce various seismic signals. In addition to impulsive events corresponding to regular earthquakes, weak nearly continuous signals without clear onset are recorded by seismographs in different environments and are known as seismic tremors. So far, seismic tremors have been reported in association with volcanoes (e.g., Konstantinou and Schlindwein, 2002; Chouet and Matoza, 2013), seismogenic faults (e.g., Obara, 2002; Nadeau and Dolenc, 2005), glaciers (e.g., Podolskiy and Walter, 2016), geysers (e.g., Kedar et al., 1996, 1998), geothermal fields (e.g., Leet, 1988; Gudmundsson and Brandsdóttir, 2010) and rivers (e.g., Burtin et al., 2011; Gimbert et al., 2014).

Volcanic tremors form the most prominent class of signals in terms of their duration recorded by seismometers installed in the vicinity of active volcanoes. They represent seismic records of continuous or nearly continuous ground vibrations with durations from minutes to months. Signals classified as tremors are recorded at most active volcanoes in association with eruptions and their preparatory phases, and sometimes during inter-eruptive periods. For this reason, tremors are one of the main focuses of volcano seismology and are used by many volcano observatories to monitor and forecast volcanic activity. Another reason for the strong interest in tremors is that the origin of most of them is believed to be directly related to processes occurring in the magmatic feeding systems. Therefore, studying the variations in the properties of observed tremor signals potentially might help us to understand how the magma is stored and migrates beneath volcanoes, which is one of the main goals of volcanology.

For the abovementionned reasons, the volcanic tremors have been extensively studied with more than 1,000 scientific papers being published on this topic up to date (Zobin, 2011). Nevertheless, despite such strong attention, many aspects of volcanic tremors remain not well understood. The main reason for this is the complexity of the phenomena. Indeed, volcanic tremor is not just one very specific type of signal produced by one specific phenomena, but a very broad (and not exactly defined) class of signals. These include: co-, pre- and inter-eruptive tremors; shallow and deep tremors; harmonic and spasmodic tremors; short-, long- and very-long-period tremors; gliding tremors, etc. Amplitudes, durations, and frequency contents of these signals are very variable. Extended reviews of properties of volcanic tremors observed at many volcanoes can be found in several dedicated papers and textbooks (e.g., McNutt, 1992; Konstantinou and Schlindwein, 2002; Chouet, 2003; McNutt and Nishimura, 2008a; Zobin, 2011; Wassermann, 2012; Chouet and Matoza, 2013).

A variety of physical mechanisms has been suggested to explain the generation of seismo-volcanic tremors. Most of them are associated with the magmatic and/or hydrothermal fluids. A non-exhaustive inventory of those includes: fluid-driven cracking (e.g., Aki et al., 1977; Aki and Koyanagi, 1981), resonance of magma filled chambers, conduits, and cracks (e.g., Chouet, 1996), nonlinear excitation by a non-stationary fluid flow (e.g., Julian, 1994), reaction force from ejected magma (Nishimura et al., 1995), magma-wagging oscillation (Jellinek and Bercovici, 2011), non-stationary transfer of gases through a permeable cap (Girona et al., 2019), magmatic–hydrothermal interactions (Matoza and Chouet, 2010), magma degassing (Melnik et al., 2020), etc. Alternatively, frictional processes have been suggested to explain the tremor origin (e.g., Iverson et al., 2006; Dmitrieva et al., 2013; Bean et al., 2014).

Ideally, the physical models of tremors could help us to use the measured properties of tremor signals to infer parameters of magmatic systems and ongoing processes such as conduit and crack dimensions, pressures and forces, gas fractions, discharge rates, etc. However, such refined interpretations of tremor observations can only be achieved in a very limited number of studies. In addition to uncertainties of tremor source physical models, one of the main obstacles is the complexity of tremor signals. Indeed, those are often composed of the contribution from multiple sources potentially activated simultaneously within volcano plumbing systems and they can be contaminated by other types of signals such as earthquakes and environmental or anthropogenic noises. In most of the cases, seismo-volcanic tremor as a signal cannot be simply and clearly defined and associated with a particular process within volcanoes. Interpretation of tremors strongly depends on the type of volcano and its activity, and often on the location of seismometers used for their observations. Because of this complexity, the cases when tremors could be successfully interpreted cannot be simply generalized or applied to different volcanic systems.

Despite of the mentioned difficulties with their interpretation, seismo-volcanic tremors are actively used as empirical indicators of volcanic activity by most of volcano monitoring observatories. In many

cases, the recording of sustained tremor is one of the main manifestation of ongoing eruption (e.g. Battaglia et al., 2005a; Senyukov et al., 2015; Battaglia et al., 2016; Duputel et al., 2021). Also, there have been attempts to use tremor amplitudes to empirically estimate lava outputs and eruption sizes as well as fountain and plume heights (e.g., McNutt and Nishimura, 2008a; Battaglia et al., 2005b; Ichihara, 2016; Fee et al., 2017). Additionally, changes of eruptive and, more generally, volcanic activity can be tracked based on variations of tremor properties. In practical terms, this often implies that a volcano observatory establishes some kind of more refined classification with different types of tremors possibly reflecting different eruptive processes. A more advanced approach is to develop automatic classification schemes based on Machine Learning (ML) (e.g., Unglert and Jellinek, 2017; Soubestre et al., 2018; Titos et al., 2019).

Following the general tendency of the rapid development of observational and information technologies, the capacities of seismo-volcanic monitoring are constantly evolving. More and more volcanoes are now instrumented with networks of modern digital seismographs. The data are recorded continuously and many observatories make them openly available, often in real time. Also, the computational resources available at volcano observatories become more powerful. These developments provide us with new possibilities to better detect, analyze, and interpret different types of seismo-volcanic signals, including tremors. Comprehensive analysis of the newly available large volumes and flows of monitoring data also poses a significant challenge that requires developing new data processing methods. To be successfully applied in the modern volcano monitoring, these methods should be able to efficiently analyze data from seismic networks of arbitrary dimensions and geometries, and be easily transportable between different volcanic settings.

With this in mind, the goal of the present chapter is not to provide an exhaustive review of all previously published methods and research results concerning volcanic tremors, but to describe a framework for network-based analysis of tremors. In section 2, we describe the content and properties of seismo-volcanic signals. Section 3 presents a brief reminder of the main single-station approaches for characterizing volcanic tremors. Section 4 shows how the amplitude of tremor recorded across a seismic network can be used to locate its source position. In section 5, we discuss how tremors and their travel times emerge when analysing inter-station covariances (cross-correlations). Section 6 presents a method based on the network covariance matrix. In section 7, we show two examples of the analysis and interpretation of volcanic tremors based on the covariance matrix method. Finally, in section 8, we discuss possible future directions to improve the network-based analysis of volcanic tremors.

2 Seismograms recorded in the vicinity of volcanoes

A seismograph installed in the vicinity of a volcano records all types of seismic signals existing elsewhere and, in addition to this, the waves generated by seismo-volcanic sources. Therefore, the recorded signal (displacement u) can be written as:

$$u = u^{amb} + u^{ant} + u^{tect} + u^{volc} + u^{inst} \tag{1}$$

where u^{amb} and u^{ant} are the natural and the anthropogenic components of the ambient noise wavefield, respectively, u^{tect} are signals generated by tectonic sources not related to the volcano-magmatic activity, u^{volc} is the wavefield generated by different types of seismo-volcanic sources, and u^{inst} is the instrumental noise. Thus, the first step in seismo-volcanic analyses is the "detection" aimed at separating the "useful" part u^{volc} from other contributions (ambient, tectonic, instrumental). This is not a fully trivial task because different terms in equation (1) can be active simultaneously and overlap in frequencies.

Nevertheless, the most important goal of volcano-seismological analysis is to interpret u^{volc} in order to infer information about the state of the volcano and processes occurring in the volcano-plumbing system. Seismo-volcanic signals are well known to be very variable in terms of time signature and frequency content (e.g., Kumagai, 2009; Chouet and Matoza, 2013). This gives rise to multiple classification schemes (see example in Figure 1), with most frequently used categories are: volcano-tectonic (VT) earthquakes, long-period (LP) events (alternatively called as low-frequency (LF) events), tremors, very-long-period (VLP) events, hybrid events, explosions, and rockfalls. Different classes of signals are, then, related to different types of seismogenic sources and volcano-magmatic processes that are responsible for their excitation.

This detection-classification-interpretation approach is dominant in volcano seismology and figures similar to Figure 1 can be found in many textbooks, review papers, and websites. Catalogs of classified seismo-volcanic events were initially created "manually" by the staff of volcano observatories. Since a few decades, a significant effort has been done in developing automated algorithms for the detection-classification, with many promising results obtained with ML approaches (e.g., Maggi et al., 2017; Cortés

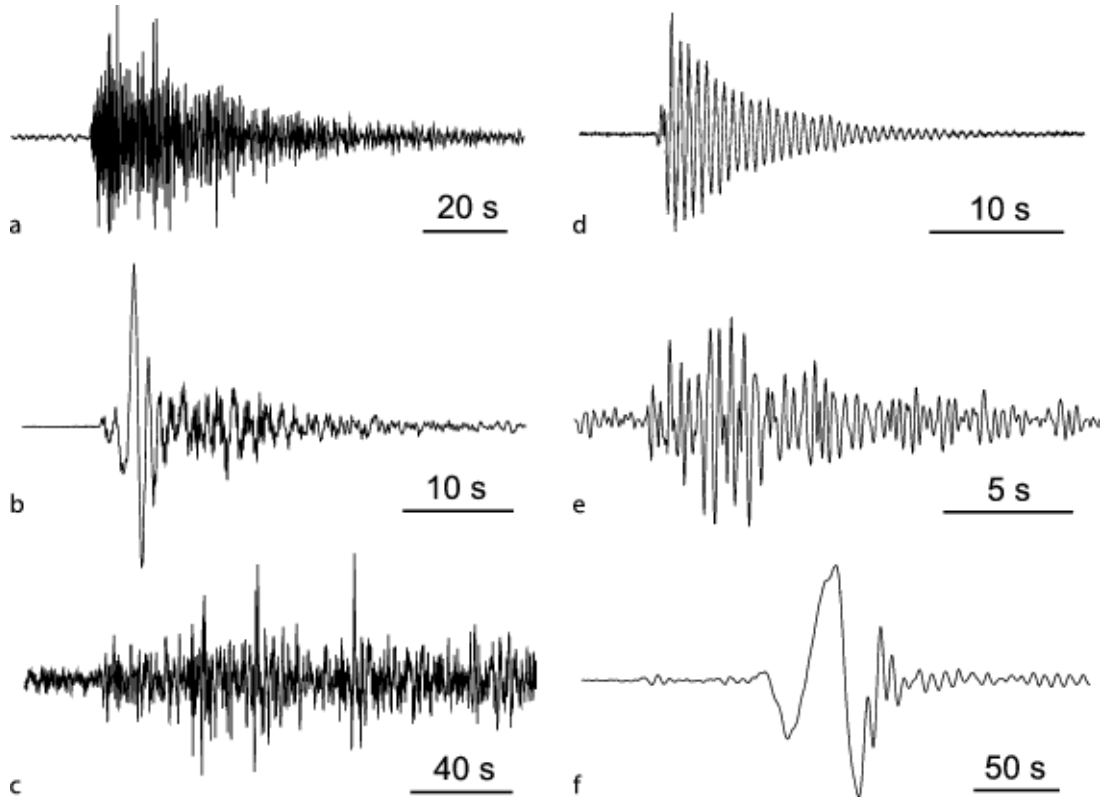

Figure 1: **Example of a classification of seismo-volcanic signals.** Reproduced from Kumagai (2009). (a) Volcano-tectonic earthquake that occurred between Miyakejima and Kozujima, Japan; (b) Explosion earthquake observed at Asama volcano, Japan; (c) Tremor that occurred beneath Mt. Fuji, Japan; (d) Long-period event observed at Kusatsu–Shirane volcano, Japan; (e) Long-period event observed at Guagua Pichincha volcano, Ecuador; (f) Very-long-period event that occurred beneath Miyakejima, Japan (low-pass filtered at 20s).

et al., 2021).

An implicit idea of classifications such as the one represented in Figure 1 is that the seismograms can be divided in reasonably short windows dominated by one type of signal/source and, therefore, corresponding to a particular type of process occurring in volcanoes. An obvious simplification of this approach is the assumption of a single source/process acting at a given time. This assumption might be reasonable for impulsive signals such as earthquakes excited by short-duration processes, i.e., brittle failure for VT earthquakes or short-living crack resonance for LP events (e.g., Chouet, 1996). Consequently, the classifications (both manual and automatic) work rather well for impulsive seismo-volcanic events. However, even for short impulsive signals, classes of "mixed" events such as hybrid events likely reflecting both brittle and fluid processes (e.g., Lahr et al., 1994) are often introduced.

The classification is much more problematic with seismo-volcanic tremors. So far, depending on its variability in time, tremor can be either continuous or intermittent. The latter can be classified as spasmodic (e.g., Ryall and Ryall, 1983) or banded (e.g. Fujita, 2008; Cannata et al., 2010). The spectral content of tremors is also very variable, with reported frequencies going from less than 1 Hz to more than 20 Hz. Additionally, tremors can be either relatively wide-band or harmonic with very narrow spectral lines. Simultaneous occurrence of different types of tremors generated by different sources are often observed (e.g., Soubestre et al., 2021; Journeau et al., 2022). Moreover, tremors can be accompanied by impulsive volcanic earthquakes. This creates a very strong diversity of tremor signals that cannot be classified into a single category as it could be suggested by Figure 1. Classifying volcanic tremors into a few simple categories does not work either.

An important property of volcanic tremors is that they typically have durations much longer than a few tens of seconds and, therefore, reflect relatively slow evolutions of volcano-magmatic systems at time scales from hours to months. Two examples of long-duration tremors are shown in Figure 2. The first one has been recorded during the July-August 2017 eruption (from 2017-07-13 to 2017-08-27) of Piton de la Fournaise volcano at La Réunion island. This was a typical flank (rift-zone) eruption (Dumont et al.,

2021) of this basaltic hot-spot volcano with a rather long duration (46 days). We show in Figures 2a and 2b two-day-long records corresponding to its beginning and terminal phases, respectively. We can clearly see that the tremor signal does not remain stationary during the eruption, which was preceded by a swarm of volcano-tectonic earthquakes (Figure 2c). The tremor amplitude is not constant and, in particular, it increases at the eruption onset (Figure 2d) and then decreases shortly after it (Figure 2a). The tremor is continuous at the beginning of the eruption (Figure 2e), while it becomes strongly intermittent at the end of the eruption when it appears as a sequence of very closely occurring LP events (Figure 2f).

The second example (Figure 2g) shows two days of continuous seismic signal recorded in the vicinity of Klyuchevskoy volcano in Kamchatka, Russia, in mid-March 2016. This volcano is known for its both co- and inter-eruptive long-duration tremors (Gordeev et al., 1990; Droznin et al., 2015; Soubestre et al., 2018, 2019). The considered two-day period corresponds to a preparatory phase of an eruption that started on April 6, 2016. During this period, both shallow and deep tremor sources were active (Journeau et al., 2022). The resulting tremor is very non-stationary. Also, continuous records in the very active Kamchatka subduction zone contain many signals from regional tectonic earthquakes (Figure 2h).

In conclusion, the volcanic tremors cannot be classified as a simple category (or a set of simple categories) of signals. Instead, they should be considered as long-duration episodes of sustained and often non-stationary seismo-volcanic activity. The non-stationarity of volcanic tremors reflects the non-stationarity of physical processes occurring in volcanic systems, that are schematically illustrated in Figure 3. Magmatic feeding systems beneath volcanoes extend over large range of depths down to the upper mantle (e.g., Cashman et al., 2017), with magma storages present at different levels. During the volcanic crises (including eruptions and their preparation phases), these systems are destabilized at different levels. As a result, multiple processes such as magma and fluid pressure transport, degassing, and fracturing are activated nearly simultaneously and often at different locations within the system. Interplay between these processes gives rise to sometimes very complex scenarios that are reflected in the complexity of the observed seismo-volcanic tremors.

In a most general case, a time (t) dependent distribution displacement $u_i^{volc}(\mathbf{r}_r, t)$ associated with seismo-volcanic sources recorded on the component i of a receiver located in $\mathbf{r}_r$ (the subscript r stands for receiver) can be written as (Kumagai, 2009):

$$u_i^{volc}(\mathbf{r}_r, t) = \int_{-\infty}^{+\infty} \iiint_V f_j^{volc}(\mathbf{r}, \tau)\ G_{i,j}(\mathbf{r}_r, t-\tau, \mathbf{r}, 0)\ dV(\mathbf{r})\ d\tau \tag{2}$$

where $f_j^{volc}(\mathbf{r}, \tau)$ is a time and space dependent equivalent body force (j - component) and $G_{i,j}(\mathbf{r}_r, t-\tau, \mathbf{r}, 0)$ is the Green's function, i.e., the mathematical representation of the seismic wave propagation from the source to the station. For volcanic earthquakes, the force distribution can be considered as a point source located in $\mathbf{r}_s$ (the subscript s stands for source) corresponding either to a single force or to a seismic moment tensor (Kumagai, 2009). In this case, and considering an elastic approximation for seismic waves, the recorded displacement can be schematically represented by a time convolution:

$$u^{volc}(\mathbf{r}_r, t) = \int_{\tau_s}^{\tau_s+\delta\tau} S^{volc}(\mathbf{r}_s, \tau)\ \tilde{G}(\mathbf{r}_r, t-\tau, \mathbf{r}_s, 0)\ d\tau \tag{3}$$

where τ_s and $\delta\tau$ are the event starting time and duration, respectively, $S^{volc}(\mathbf{r}_s, \tau)$ is a generic representation of a source time function that can be either a force vector or a moment tensor, and $\tilde{G}(\mathbf{r}_r, t-\tau, \mathbf{r}_s, 0)$ represents either the Green's function or its spatial derivative.

Equation (3) is not applicable in the case of seismo-volcanic tremors for two reasons. First, the tremor source time functions are not localized in a short interval $\delta\tau$ but rather have long durations and often complex variability in time. Second, as discussed above, many records of seismic tremors contain signatures of different sources acting simultaneously. Therefore, the most general case of seismic tremor should be described with a full equation (2). In the case of a few tremor sources remaining stationary in space within the considered time window, it can be simplified as:

$$u^{volc}(\mathbf{r}_r, t) = \sum_k \int_{-\infty}^{+\infty} S^k(\mathbf{r}_s^k, \tau)\ \tilde{G}(\mathbf{r}_r, t-\tau, \mathbf{r}_s^k, 0)\ d\tau \tag{4}$$

where k indexes different acting tremor sources located in positions $\mathbf{r}_s^k$.

Within the framework introduced above, an ideal goal of the analysis of seismic tremors could be formulated as retrieving the full source time function $f_j^{volc}(\mathbf{r}, \tau)$ appearing in equation (2). This is, however, not feasible because of the limited number of recording stations, the contamination by non-volcanic signals, and the poorly known subsurface structure (the Green's functions). Therefore, the

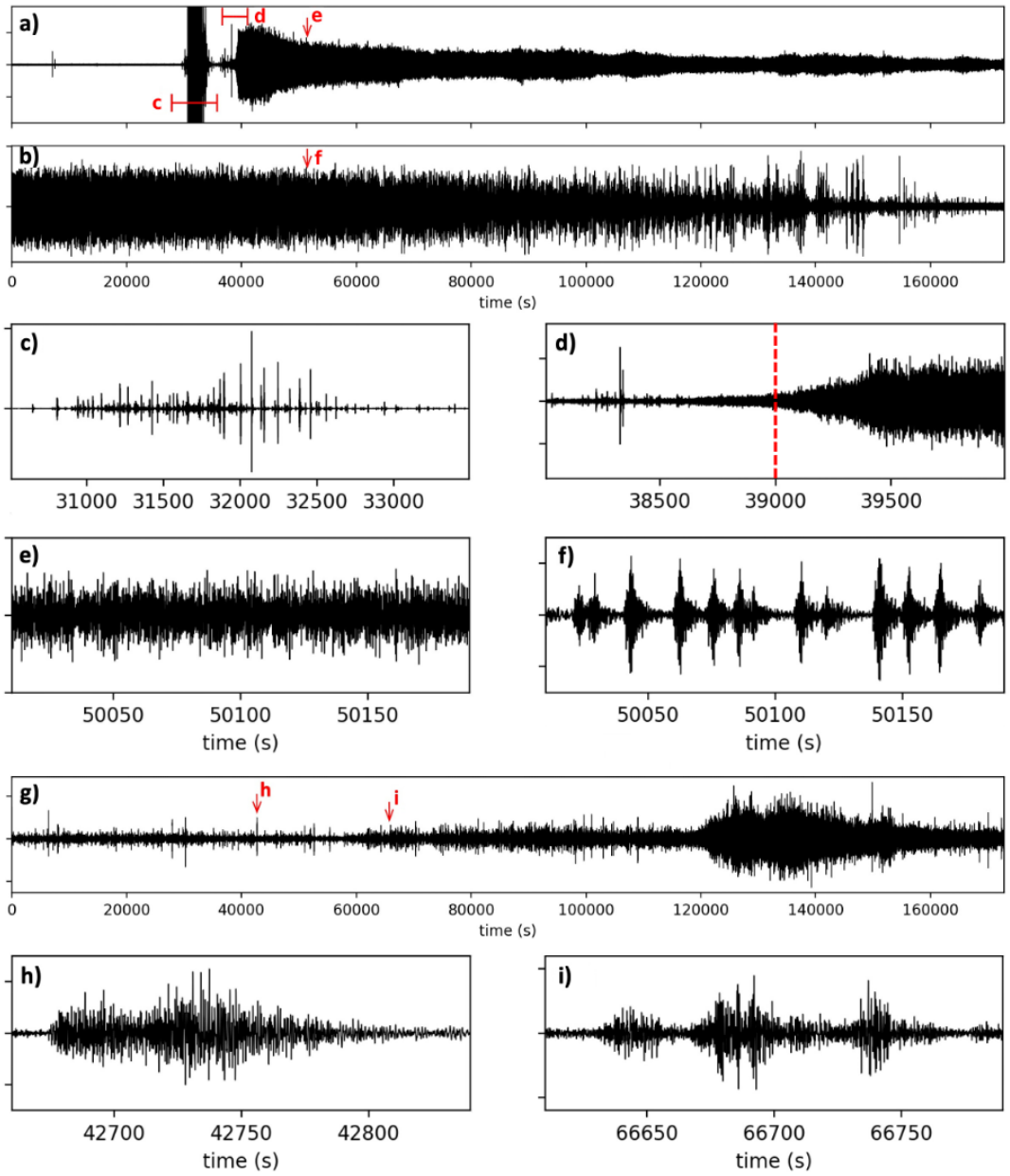

Figure 2: **Examples of seismograms recorded on volcanoes**. Normalized vertical component velocities bandpassed between 0.5 and 25 Hz are shown. (a) and (b) Two-day-long seismograms containing long-duration tremors emitted during the July-August 2017 eruption (from 2017-07-13 to 2017-08-27) of Piton de la Fournaise volcano (PdF) recorded by station RVL (Piton de la Fournaise Volcano Observatory Network, doi:10.18715/REUNION.PF) located ∼1 km south-west of the main crater. (a) Beginning of the eruption (seismogram starting time: 2017-07-13 10:00 UTC). (b) Terminal phase of the eruption (seismogram starting time: 2017-08-26 00:00 UTC). (c)-(f) Zoomed view on portions of signals indicated with red letters in (a)-(b). (c) Swarm of volcano-tectonic earthquakes preceding the July-August 2017 PdF eruption. (d) Emergence of eruptive tremor associated with the onset of the eruption indicated with a red vertical dashed line. (e) 180 sec of continuous tremor during the initial phase of the eruption. (f) 180 sec of intermittent tremor during the terminal phase of the eruption. (g) Two-day-long seismogram recorded in mid-March 2016 by station SV13 (temporary experiment KISS, Shapiro et al. (2017b), doi:10.14470/K47560642124) located ∼4.5 km north of the main crater of Kyuchevskoy volcano in Kamchatka, Russia (seismogram starting time: 2016-03-14 10:00 UTC). (h)-(i) Zoomed view on portions of signals indicated with red letters in (g). (h) Regional subduction-zone earthquake in Kamchatka. (i) 180 sec of intermittent tremor associated with the Klyuchevskoy activity.

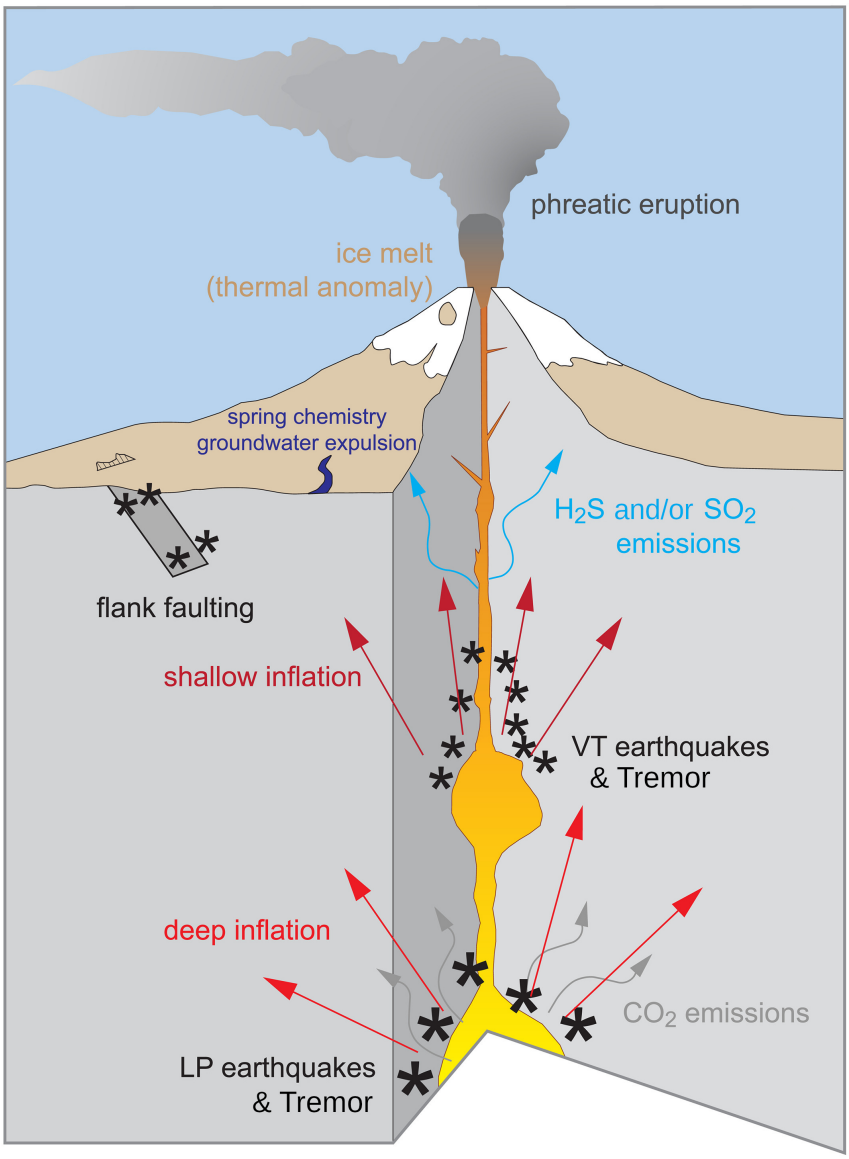

Figure 3: **Idealized representation of a generic stratovolcano showing various types of volcanic processes and possible associated seismo-volcanic sources.** Modified from Poland and Anderson (2020).

tremor analysis can be more reasonably formulated based on equation (4). In this case, the first goal of the analysis is to identify the principal tremor sources active during the considered period of volcanic activity. This should be followed by characterizing the source time functions $S^k(\mathbf{r}_s^k, \tau)$. Their exact retrieval is again not feasible. However, with appropriate data coverage, an approximate characterisation of slow varying properties (location in space and frequency content) can be obtained, as we will discuss in the following sections.

3 Single station analysis

Despite the rapid development of networks of instruments on many volcanoes in the World, methods based on a single station remain very important for volcano monitoring at volcano observatories with limited resources, because of the simplicity of their implementation and their robustness.

3.1 Tremor amplitudes at a single station

The simplest approach for characterizing seismo-volcanic signals consists of computing the average signal amplitude in a moving window (typically a few minutes long) on a single component of a single station.

The most used method is called Real-time Seismic Amplitude Measurement (RSAM) (Endo and Murray, 1991) and its variants are implemented in most of volcano observatories. This approach has the advantage of simplicity. It does not require a dense network of instrumentation and can be implemented even with old-type analogous seismic recorders. As a consequence, the single-station average amplitude estimation is very robust.

Despite its simplicity, the RSAM method gives a very useful overall view of the seismo-volcanic activity and, in particular, of volcanic tremors. It is often used as the main indicator (in the absence of visual observation) of the beginning and the end of an eruption. This is illustrated in Figure 4 that shows the RSAM computed during the June 2019 eruption of the Piton de Fournaise volcano at La Réunion Island. This relatively short eruption started at 02:35 UTC on June 11, 2019 as very clearly seen in the RSAM plot and remained active approximately till 08:00 UTC on June 13.

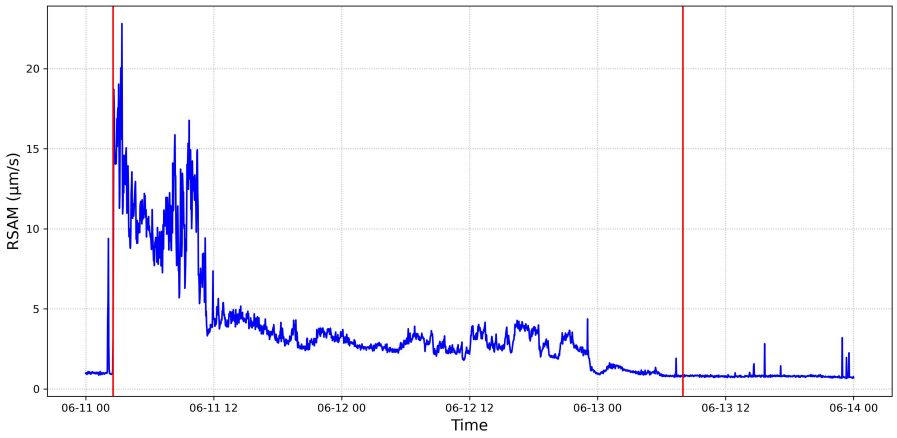

Figure 4: **Example of RSAM computed from a co-eruptive tremor.** RSAM evolution computed between 2019-06-11 00:00 and 2019-06-14 00:00 UTC at seismic station DSO (Piton de la Fournaise Volcano Observatory Network, doi:10.18715/REUNION.PF), using vertical component and filtering between 0.5 and 10 Hz. The two vertical red lines indicate the beginning and the end of the eruption, respectively.

Also, there have been a few attempts to establish a scaling between the tremor amplitude and the eruption size (McNutt, 1994), based on measuring the reduced displacement (Aki and Koyanagi, 1981) that represents a maximal tremor amplitude corrected for geometric spreading (amplitude times distance) and instrument gain. The tremor reduced displacement has been reported to roughly scale with both the ash column height and the volcanic explosivity index (VEI) (Newhall and Self, 1982), as well as with the square root of the cross sectional area of the eruptive vent (McNutt and Nishimura, 2008b). A recent study confirms the existence of a relationship between tremor amplitudes and eruption plume height as well as eruption duration (Mori et al., 2022). On the other hand, this relationship between tremor amplitude and plume height is not applicable for all volcanoes, as for example during the 2010 Eyjafjallajökull eruption (Iceland) when a drop in seismic tremor was observed while the plume height increased (Gudmundsson et al., 2010), or energetic banded tremor was not coinciding with elevated plume height (Caudron et al., 2022). Similarly, the relationship between seismic tremor amplitude and eruptive duration is not always verified. The recent 2021 Fagradalsfjall eruption (Iceland) was characterized by a seismic tremor whose amplitude did not correlate with the eruptive lava fountain episode duration, but with the duration of the repose time between those eruptive episodes (Eibl et al., 2023).

Moreover, power law scaling relations between tremor amplitudes and magma discharge rate have been proposed with different power indices based on various data sets reviewed by Ichihara (2016). However, this kind of scaling remains empirical and might lead to erroneous estimations when applied without identifying the tremor origin (e.g., shallow vs. deep), or if more than one tremor source is active at the same time (Eibl et al., 2017a).

While being very useful for the real-time monitoring, the measurement of tremor amplitudes at a single station is not sufficient to analyze the complexity of tremor and to separate possible different sources (equation 4). Therefore, other signal properties such as spectral content and polarization should be used for a more advanced analysis, as detailed in the following sections.

3.2 Spectral content of tremor at a single station

Different types of volcanic tremors have distinct spectral properties. While some of them are rather broadband, others have spectra consisting of one or several sharp peaks (these latter are most likely related with the excitation mechanisms involving internal resonances in the plumbing systems). Therefore, the spectral analysis is a very powerful tool for distinguishing different tremor types and their sources. As discussed in section 2, the properties of seismo-volcanic tremors vary in time following the changes occurring within the plumbing systems. Therefore, these changes are reflected by variations of the tremor spectral content in time and can be tracked by applying a time-frequency analysis.

A spectrogram of two days of seismic tremors recorded near the Klyuchevskoy volcano (Kamchatka, Russia) is shown in Figure 5. It clearly demonstrates that, in addition to variations of tremor amplitudes, its spectral characteristics are changing over time. During the initial 60,000 sec (16.7 hrs) of this record, the tremor is dominated by relatively low frequencies with a few clearly distinguishable spectral lines. Several impulsive events on top of this tremor are observed and most likely correspond to tectonic earthquakes (Figure 2h). Then, between 60,000 and 120,000 sec (16.7 and 33.3 hrs), the amplitude of the tremor slightly increases while its spectral characteristics do not change significantly. This might indicate that during this period of volcanic activity, the tremor was generated by the same source and process with slightly increasing intensity after the first 16.7 hours (60,000 sec). Conversely, after 120,000 sec (33.3 hrs), the strong increase of the tremor amplitude is also accompanied by a significant variation of its spectral properties, with appearance of high-frequency (>10 Hz) energy and more significant time intermittence seen as vertical bands on the spectrogram. These changes likely indicate that the tremor origin has been modified after the initial 33.3 hours (120,000 sec) of the record. The fact that low-frequency (between 1 and 3 Hz) spectral lines are still observed might indicate that the generating mechanism that has been acting during the first 33.3 hours still persists and that an additional source/process generating higher frequency tremor is activated.

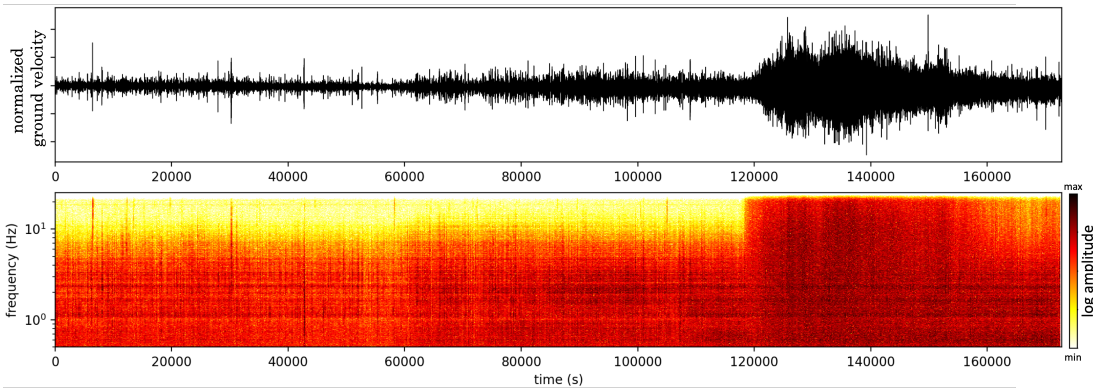

Figure 5: **Example of a tremor spectrogram.** Upper frame shows a two-day-long tremor record at the Klyuchevskoy volcano in Kamchatka, Russia (same as Figure 2g, seismogram starting time: 2016-03-14 10:00 UTC), whose spectrogram is shown below (bandpassed between 0.5 and 5 Hz).

While the time-frequency analysis is a very efficient tool for detecting changes in the composition of the signal recorded at a single component that might be caused by variations of the tremor generating mechanism, its interpretation is rather ambiguous. One important reason for this ambiguity is that the location of the tremor source cannot be inferred from the one-component signal. A second reason is that the source and the propagation effects are not easy to separate based only on single station records. So far, the low-frequency spectral lines seen in Figure 5 could be attributed either to sources properties, or to interaction of seismic waves with the near-station structure, i.e., the so-called site effect (e.g., Fehler, 1983; Goldstein and Chouet, 1994; Konstantinou and Schlindwein, 2002), or to the scattering on structural heterogeneities (Barajas et al., 2023).

3.3 Polarization of tremor signal at a single station

If a tremor generating seismic source remains at the same location and with a constant mechanism, the emitted seismic waves will be characterized by a constant (even possibly complex) polarization. This polarization expresses itself as a particular correlation between ground motions recorded at different components of a single station (one vertical and two horizontals). Therefore, it can be analyzed when records with three-component stations are available.

A simple approach to detect a persistent polarization in continuous signals is to analyze the single-station inter-component cross-correlation function of one pair of components (EN, EZ or NZ). For a seismic noise generated by randomly distributed sources, these cross-correlations computed over relatively short time windows are random and variable in time. On the contrary, for a signal generated by a persistent tremor source they remain stable in time. This stability of the inter-component cross-correlation function can be characterized by comparing results from consecutive time windows resulting in an efficient tremor detector (Journeau et al., 2020, 2022). Additionally, the waveform of the cross-correlation function can be used as a "fingerprint" of a particular tremor source (Droznin et al., 2015) and helps to separate different tremor generating processes.

A more advanced polarization analysis is performed with using the full set of inter-component cross-correlations (cross-spectra) at a single station, that forms a 3x3 covariance matrix (Vidale, 1986). This matrix is complex and Hermitian and its three eigenvalues are real, while eigenvectors are complex. The ratio between eigenvalues can be used to determine the degree of polarization. When a single eigenvalue is much larger than the two remaining ones, a single wave is dominating the signal. When no dominating eigenvalue is observed (the three eigenvalues are of the same order of magnitude), the signal represents a mixture of different types of waves. For a dominating wave, the respective eigenvector can be analyzed in the framework of the "complex polarization analysis" (e.g., Vidale, 1986; Levshin et al., 1989) in order to determine the type of polarization (linear vs elliptical) and to measure parameters such as the backazimuth and the incident angle of the polarization vector. Polarization analysis has been applied to volcanic tremors in the time (e.g., Konstantinou and Schlindwein, 2002; Ereditato and Luongo, 1994), frequency (e.g., Chouet et al., 1997), and time-frequency (e.g., Haney et al., 2020) domains. The latter approach is more selective and better separates different signals. Thus, Haney et al. (2020) studied the seismic tremor recorded during eruptive activity over the course of the 2016–2017 eruption of Bogoslof volcano, Alaska, with applying the time-frequency polarization analysis to three-component seismic data and found that it was dominated by P-waves. This information helped the authors to improve estimates of average reduced displacement.

3.4 Identifying different types of volcanic tremors with machine learning at a single station

The methods described in the previous paragraphs can be very efficiently applied to continuous seismic records to estimate tremors amplitudes, spectral characteristics, and polarization properties. Based on these measurements, it is possible to identify different types of tremors, possibly corresponding to different processes/locations within the volcano plumbing system. For a relatively short tremor episode, this kind of inferences can be done with a visual inspection of the analysis results. However, in most cases when tremor remains for several days or months, the amount of information to account for becomes too large and its unbiased analysis requires more formal and automated approaches. As in many other disciplines, ML approaches are becoming very popular in volcano seismology for automatic classification of signals and pattern recognition (e.g., Titos et al., 2019; Cortés et al., 2021).

Supervised "classification" of volcanic tremors would consist in training algorithms like neural networks, random forest, support vector machines, or others, based on "labeled" waveforms of different types of tremors. In other words, this approach requires an a priori information about possible properties of tremor signals. As explained in section 2, the a priori classification of tremor signals is rather problematic because of the huge variability of possible combinations of many types of tremors.

Therefore, unsupervised methods are better adapted for the analysis of continuous seismo-volcanic tremors. In most cases, this implies applying various "clustering" algorithms to group tremor signals based on their distinct amplitudes and spectral characteristics (and eventually polarization properties). Unglert et al. (2016); Unglert and Jellinek (2017) have demonstrated that clustering algorithms existing in modern ML toolboxes (such as Principal Component Analysis, Hierarchical Clustering, Self Organized Maps) applied to single station data can efficiently detect volcanic tremors or other types of seismo-volcanic signals (such as earthquakes and lahars) and identify their types. Hence, unsupervised volcanic tremor classifiers are generally using single-station based signal features, such as RSAM time series (Steinke et al., 2023), spectra (Unglert et al., 2016; Unglert and Jellinek, 2017) or single-station inter-component cross-correlation functions (Yates et al., 2023; Makus et al., 2023). Such ability to rapidly group tremors without prior knowledge about the character of the seismicity at a given volcanic system holds great potential for real time or near-real time applications, and thus ultimately for eruption forecasting. At the same time, interpreting the origin of the observed groups of tremors based on results from a single station remains problematic because of the unknown location of their sources and the difficulty in separating source and propagation effects.

4 Amplitude-based network analysis of seismo-volcanic tremors

As mentioned in the previous section, one of the main shortcomings of single station methods is their impossibility to determine the location of the tremor source. This location can be found based on simultaneous analysis of records at several seismic stations, or, in other words, of a seismic network. A set of methods is based on measuring the tremor amplitudes at different stations and finding the source position that better predict the decay of these amplitudes with propagation distance.

The *Amplitude Source Location (ASL)* method was developed by Battaglia and Aki (2003) for a configuration when a single localized and fixed tremor source dominates the recorded wavefield. The amplitude at station i is given by:

$$A_i = \frac{A_0}{\gamma_i \, d_i^{\alpha}} \, exp\left(-\pi f \int_{path_i} \frac{dl}{Qv}\right) \tag{5}$$

where A_0 is the source amplitude, the term $1/(d_i^{\alpha})$ represents the geometrical spreading with $\alpha = 1$ for body waves or $\alpha = 1/2$ for surface waves, γ_i is the amplitude correction at station i to take site effect into account, d_i is the distance from the source to station i, f is the frequency, and v, Q and dl are respectively the wave velocity, the attenuation quality factor and the incremental distance along the path from the source to the station. The attenuation quality factor Q is often estimated based on seismic coda amplification factors (Aki and Ferrazzini, 2000) measured from regional or local earthquakes. Note that for uniform velocity and attenuation, parameters v and Q are constant and $\gamma_i = 1$ (no site effect) so that equation (5) simplifies as:

$$A_i = \frac{A_0}{d_i^{\alpha}} \, exp\left(\frac{-\pi f d_i}{Qv}\right) \tag{6}$$

The tremor source is finally located at the position of a 3-D grid minimizing the misfit between calculated and observed amplitudes across the network (Gottschämmer and Surono, 2000). The method is often used in the 5-10 Hz frequency range in which, likely due to scattering phenomena, the assumption of isotropic radiation is valid and equation (6) can be used. Recent improvements of this method include the consideration of depth-dependant scattering and attenuation at Nevado del Ruiz volcano (Kumagai et al., 2019), and relative locations at Meakandake volcano (Ogiso and Yomogida, 2021).

Volcanic tremor was located with the ASL method at many different volcanoes. The first use of this method on volcanic tremor was carried out at Piton de la Fournaise, where the tracking of shallow tremor sources appeared to be an efficient tool to monitor the opening of new eruptive fissures during the 1998 and 1999 eruptions (Battaglia and Aki, 2003; Battaglia et al., 2005a). At Mount Etna, shallow tremor sources were located close to eruptive craters during pre-effusive and effusive phases of the 2004 eruption (Di Grazia et al., 2006), as well as beneath the South East Crater imaging shallow conduits where magma degassing was taking place during strombolian activity and fire fountain episodes in 2007 (Patanè et al., 2008). Still at Etna, tremor was located 1-2 km a.s.l. below the North East Crater where a magma body was cyclically feeding some fire fountains in 2011, during which the tremor source was migrating shallower towards the North South East Crater (Cannata et al., 2013; Moschella et al., 2018). Tremor-like signals generated by lahars and pyroclastic flows were tracked descending on the flanks of Cotopaxi (Kumagai et al., 2009) and Tungurahua (Kumagai et al., 2010). Shallow tremor sources were located in the old north crater, in the lava lake of the active crater and in an intermediate fumaroles field of the Erta'Ale caldera during an experiment in 2003 (Jones et al., 2012). Shallow migrations of tremor sources were observed prior to phreatic eruptions of Japanese volcanoes, with lateral migrations in 2008 at Maekandake (Ogiso and Yomogida, 2012) and descending migration (over ∼2 km) in 2014 at Ontake (Ogiso et al., 2015).

An alternative to the ASL method is the *Seismic Amplitude Ratio* method. It is based on the ratio of seismic amplitude at pairs of stations i and j. For uniform velocity and attenuation, using (6) it comes:

$$R_{i,j} = \frac{A_i}{A_j} = \left(\frac{d_j}{d_i}\right)^{\alpha} \, exp\left(\frac{-\pi f}{Qv}(d_i - d_j)\right) \tag{7}$$

The ratio $R_{i,j}$ is calculated for the different station pairs of the network and the misfit between calculated and observed ratios is minimized to find the 3-D position of the tremor source.

The first application of this method was carried out by Carbone et al. (2008) to locate tremor at Etna during the December 2005 to January 2006 non-eruptive period. The tremor source was positioned in a volume with a centroid located at 0.6 km above the sea level (∼2.2 km below the surface), a maximum length and width of about 2 and 1 km, respectively, and slightly shifted to the south of

the Summit Craters. Later, the seismic amplitude ratio method was used to image the dynamics of dyke propagation in real time during the January 2010 Piton de la Fournaise eruption (Taisne et al., 2011). In Kamchatka, migrations of tremor sources were interpreted as magma movements prior to the 2012–13 Tolbachik eruption (Caudron et al., 2015). In Iceland, the amplitude ratio method was combined with both array-based azimuth determination and 3-D seismic full wavefield elastic numerical modelling to constrain a migrating pre-eruptive tremor location to the uppermost 2 km of the crust above the propagating dyke at Bardarbunga in 2014 (Eibl et al., 2017b). This pre-eruptive tremor was attributed to swarms of microseismic events associated with fracturing during the dyke formation, with seismically silent subsequent magma flow in the newly formed dyke. An exception occurred on September 3, 2014, when the tremor was located beneath ice cauldrons located 12 km south of the ongoing eruptive site, as confirmed later by another study (Caudron et al., 2018). In Japan, tremor sources associated with phreatomagmatic activity at Aso volcano from December 2013 to January 2014 were found to be located in a cylindrical region of the top 400 m below the surface, interpreted as a network of fractures (Ichimura et al., 2018). Still in Japan, tremor sources were located at 0.5–1 km depth and 1 km north from Motoshirane cone ∼2 min before the 2018 phreatic eruption of Kusatsu-Shirane, possibly reflecting small shear fractures induced by sudden hydrothermal fluid injection into an impermeable cap-rock layer which triggered the eruption (Yamada et al., 2021). In New Zealand, tremor migration associated with phreatic activity was observed at Whakaari/White Island volcano (Caudron et al., 2021). In the Galápagos Islands, the sources of both pre- and co-eruptive tremor were located with the seismic amplitude ratio method during the 26 June 2018 eruption at Sierra Negra (Li et al., 2022). The pre-eruptive tremor was interpreted as generated by fracturing associated with dyke propagation, opening pathway later used for silent magma flow as already suggested at Bardarbunga (Eibl et al., 2017b). The different spectral content of co-eruptive tremor compared to pre-eruptive tremor allowed for a precise timing of the eruption onset.

5 Tremor and inter-station cross-correlations

Tremor amplitudes analyzed in the previous section to locate their sources contain only a small portion of the information. At the same time, the phase of tremor signals seems to be difficult to analyze because of its random nature. Indeed, according to equation (4), this phase is randomized by the source processes $S^k(\mathbf{r}_s^k, \tau)$. However, the randomness of the source time function can be compensated by computing cross-correlations between station pairs. To demonstrate this, let us consider a simplified case when a single tremor source is acting at position $\mathbf{r}_s$ and remains stationary in time. We then re-write equation (4) in the Fourier spectral domain as :

$$U^{tr}(\mathbf{r}_r, \omega) = S(\omega)\ \tilde{G}(\mathbf{r}_r, \mathbf{r}_s, \omega) \tag{8}$$

where $U^{tr}(\mathbf{r}_r, \omega)$ is the Fourier spectrum of the tremor signal recorded at position $\mathbf{r}_r$, $S(\omega)$ is the Fourier spectrum of the source time function, and $\tilde{G}(\mathbf{r}_r, \mathbf{r}_s, \omega)$ is the generalized Green's function in the Fourier domain.

An equivalent of the time-domain cross-correlation in the Fourier domain is the cross-spectrum, that is computed as the product between one spectrum and the complex conjugate of another. For a cross-spectrum of tremor recorded at two stations 1 and 2 (located in $\mathbf{r}_1$ and $\mathbf{r}_2$, respectively) this gives:

$$CC_{1,2}(\omega) = |S(\omega)|^2\ \tilde{G}(\mathbf{r}_1, \mathbf{r}_s, \omega)\ \tilde{G}^*(\mathbf{r}_2, \mathbf{r}_s, \omega) \tag{9}$$

In equation (9), the random source phase disappears and the resulting cross-correlation is formed by two factors. The first one is the power spectral density of the tremor source $|S(\omega)|^2$. The second factor is the cross-correlation of two Green's functions that depends on the wave propagation between the source and the two receivers. If the tremor position and mechanism do not change, this second factor remains constant. As a consequence, the inter-station cross-correlation waveform is very sensitive to modifications of the tremor source spectrum and mechanism, or to a change of its position. Therefore, it can be used as a tremor source "fingerprint".

The Earth's interior is an heterogeneous medium from the wave propagation point of view, and in particular its shallow crust in volcanic regions. In such a medium, it is convenient to consider the seismic wavefield as being composed of two contributions (e.g., Campillo and Margerin, 2010). First, "ballistic" waves propagate in a smooth slowly varying medium where the wave fronts can be perfectly tracked and wave travel times defined. The propagation of waves can then be successfully described by geometrical methods such as ray theory. On top of this smooth wavefield, the scattering on small-scale obstacles or

lateral variations of elastic parameters result in wave fronts distortion and deflection of seismic energy in all possible directions. As a result, a seismic coda is formed after the arrival of the ballistic waves.

The "ballistic" part of the Green's function can be simplistically described as a simple combination of the wave travel time $t_{r,s}$ between the source s and the receiver r positions, with the amplitude attenuation $a(\mathbf{r}_r, \mathbf{r}_s)$:

$$\tilde{G}^{bal}(\mathbf{r}_r, \mathbf{r}_s, \omega) = a(\mathbf{r}_r, \mathbf{r}_s)\ e^{-i\omega t_{r,s}} \tag{10}$$

As a result, equation (9) can be re-written as:

$$CC_{1,2}(\omega) = |S(\omega)|^2\ a(\mathbf{r}_1, \mathbf{r}_s)\ a(\mathbf{r}_2, \mathbf{r}_s)\ e^{-i\omega(t_1 - t_2)}\ +\ |S(\omega)|^2\ CC_{1,2}^{scat}(\omega) \tag{11}$$

The first term in this expression contains information about the relative propagation time from the tremor source to receivers 1 and 2 : $(t_1 - t_2)$ and, therefore, can be used to locate the source position (e.g., Ballmer et al., 2013; Droznin et al., 2015). The second term is more complex and mainly depends on cross-correlations of the scattered waves schematically denoted as $CC_{1,2}^{scat}(\omega)$. Despite its complexity, this term remains constant for a source with fixed position/mechanism and, therefore, makes the cross-correlation "fingerprinting" more selective.

We illustrate the properties of the inter-station tremor cross-correlations with an analysis of records from the monitoring seismic network operated by the Kamchatkan Branch of the Russian Geophysical Service on the Klyuchevskoy Group of Volcanoes in Kamchatka, Russia (Droznin et al., 2015). This network (Figure 6a) records tremors generated by several active volcanoes and, therefore, is very convenient for illustrating analysis of multiple tremor sources.

Examples of 1,000 sec (16.7 min) long vertical component continuous records from stations LGN and KMN are shown in Figures 6b and 6c, respectively. We show records for 3 days: 2010-03-05, when the Klyuchevskoy volcano was erupting; 2011-04-28, when all volcanoes were quiescent; and 2012-12-01, a few days after the beginning of the Tolbachik eruption. All shown records look like "random" noise and their most distinctive feature is the difference in amplitudes.

Figures 6d-f show examples of day-long cross-correlations corresponding to the three previous dates (computed between LGN, highlighted with yellow in Figure 6a, and all other stations). To minimize the contribution of strong signals such as earthquakes or calibration pulses, we followed the approach of Bensen et al. (2007) to pre-process the continuous records with applying a spectral whitening between 0.1 and 4 Hz followed by a one-bit normalization.

Cross-correlations computed during a day when all surrounding volcanoes were quiet look like random time series (Figure 6e). The result is very different during the days when Klyuchevskoy (Figure 6d) or Tolbachik (Figure 6f) volcanoes were active. During the Klyuchevskoy activity, strong one-sided signals emerge in all cross-correlations. A close inspection shows that this signal propagates from a vicinity of station LGN (closest station to the active crater of the Klyuchevskoy volcano) to all other stations. At some station pairs (e.g., KPT-LGN or CIR-LGN), we can distinguish a relatively low-frequency short arrival that corresponds to ballistic contribution in equation (11). Much broader tails containing higher frequencies correspond to "scattering" contributions. During the Tolbachik activity, we see again strong emerging asymmetric signals. However, their shapes and relative travel times are very different from those recorded during the period of the Klyuchevskoy activity. In particular, for most of the station pairs the maxima were shifted from the left to the right side, implying that the tremor source is located further from LGN than from most other stations.

Equation (9) predicts that if the position and mechanism of the tremor source as well as the medium remain constant, the irregular source time function is cancelled and the resulting cross-correlation at a given station pair remains stable in time. The scenario described above can be realized when the eruptive centre of a volcano remains in the same position during long eruptive episodes. In this case, the cross-correlation waveforms computed from different time windows during these episodes will remain stable in time. This property is illustrated in Figures 7a and 7b, that show cross-correlations computed between stations CIR and LGN during 8 consecutive days in January 2010 and in January 2013 when Klyuchevskoy and Tolbachik volcanoes erupted, respectively. During both of the 8-days periods, the cross-correlation waveforms remain very stable in time. In both cases, relatively low-frequency ballistic waves can be seen at $\sim$ -5 sec, implying that they first arrive at LGN that is closer to both eruptive centers (tremor sources). At the same time, the "scattered" contribution to the cross-correlation is much stronger during the Tolbachik eruption (Figure 7b), that is more distant relative to the considered pair of stations. This makes the cross-correlation waveforms corresponding to activities of the two volcanoes very different. The presented examples show that cross-correlations computed between a single station pair are very sensitive to the location of the source. As a result, they can be very efficiently used as

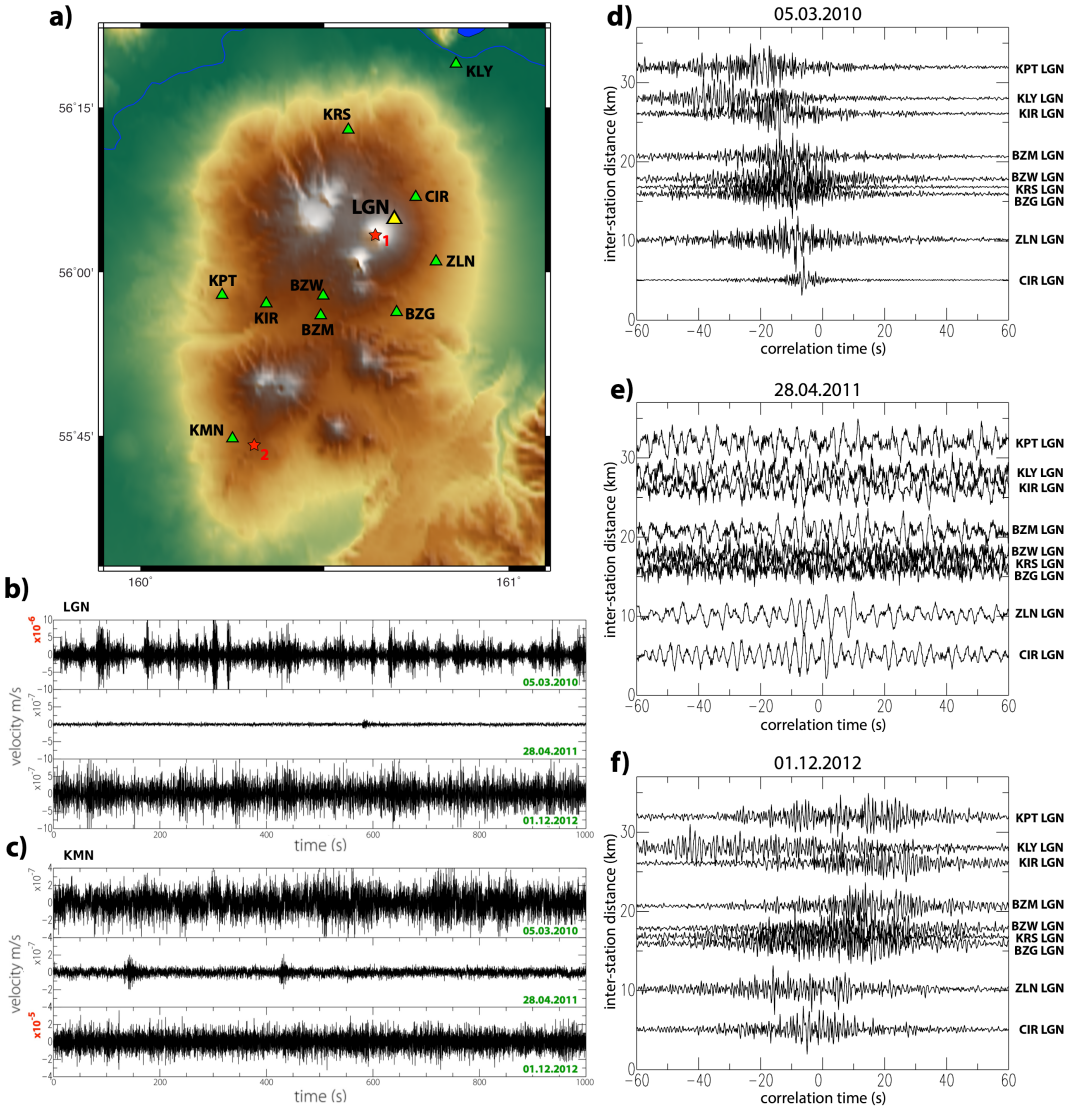

Figure 6: **Continuous time series and inter-station cross-correlation functions at the Klyuchevskoy Group of Volcanoes (KVG) in Kamchatka, Russia.** Modified from Droznin et al. (2015). Non-filtered records by short-period seismographs with corner frequency of 0.8 Hz are shown and used in the analysis. (a) KVG topographic map. Triangles show the position of seismic stations. Red stars indicate the location of the 2009–2010 Kyuchevskoy (1) and of the 2012–2013 Tolbachik (2) eruptive centres. (b) and (c) Examples of continuous records from vertical component of stations LGN and KMN, respectively. Corresponding dates are indicated with green numbers (records start at 00:00:00 UTC). Note the differences in the vertical scales as indicated with red numbers. (d)-(f) Cross-correlations of day-long vertical component records between stations LGN, shown with a yellow triangle in (a), and a set of other stations for dates illustrated in (b) and (c).

"fingerprints" of tremors emitted by particular volcanoes. Alternatively, changes in the cross-correlation waveforms can reflect some changes of the medium/topography caused by volcanic phenomena such as intrusions, growth of eruptive cones, collapses, etc.

The similarity between cross-correlation waveforms can be quantified with computing a Pearson correlation coefficient. Figures 7c and 7d demonstrate that when selecting as fingerprints cross-correlation waveforms during respective days of Kyuchevskoy and Tolbachik activity, the resulting correlation coefficients computed from sections between -40 and 40 s delineate the main periods of activity of these volcanoes. The reference cross-correlation waveforms used for this "phase-matched" detection of tremors were selected arbitrary. With this approach, the efficiency of the detection could be deteriorated if the selected "reference" date was not representative of the most typical tremors. Figure 7e shows a matrix of correlation coefficients computed between all daily cross-correlations during the period of study. This

matrix is symmetric and its rows (or columns) are equivalent to curves shown in Figures 7c and 7d, with using different daily cross-correlation waveforms as references. The structure of this matrix clearly shows the separation between the activity of Klyuchevskoy and Tolbachik and, in addition, the possible existence of several clusters of similar cross-correlation waveforms likely corresponding to different sources of volcanic tremors. A more detailed analysis of these clusters and of the identification of their sources is presented in the following sections.

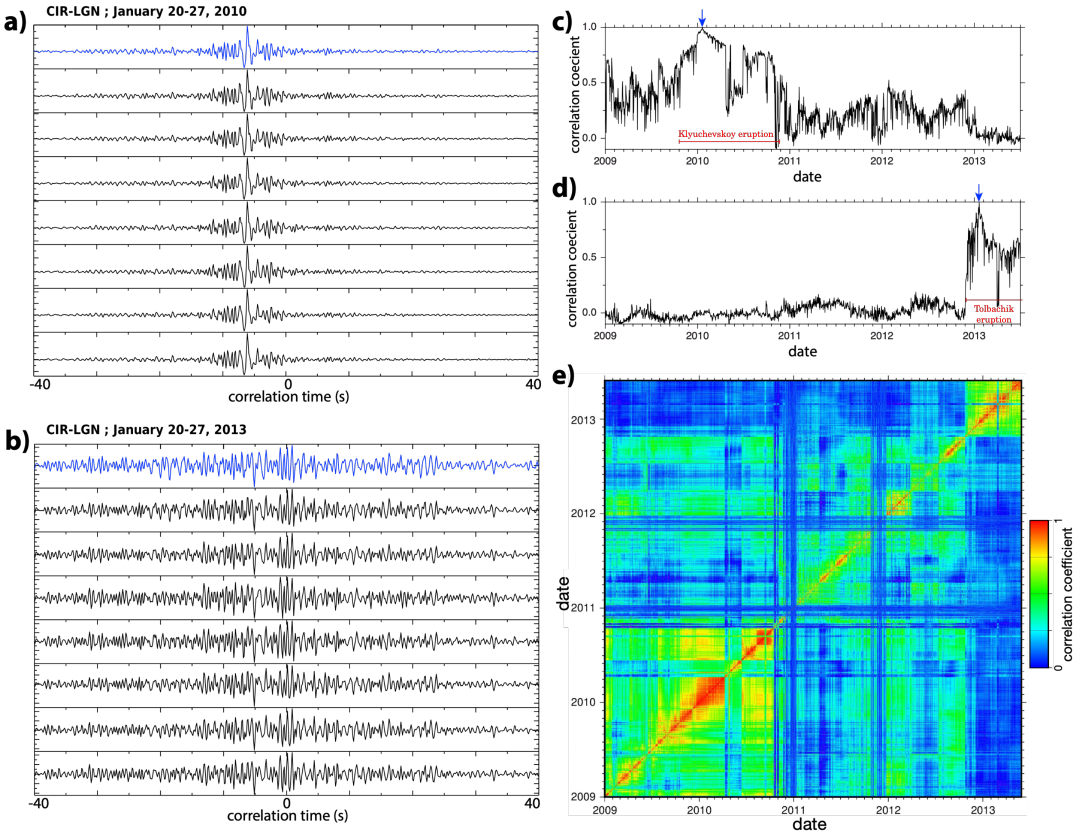

Figure 7: **Cross-correlations as fingerprints of volcanic tremor sources.** Modified from Droznin et al. (2015). (a) Daily cross-correlations for station pair CIR-LGN during the Klyuchevskoy eruption: between January 20 and January 27, 2010. (b) Daily cross-correlations for station pair CIR-LGN during the Tolbachik eruption: between January 20 and 27, 2013. (c) Correlation coefficient between all daily cross-correlations and the reference cross-correlation waveform corresponding to the Klyuchevskoy eruption (the cross-correlation on January 20, 2010 shown with the blue colour in (a) and indicated with the blue arrow). (d) Correlation coefficient between all daily cross-correlations and the reference cross-correlation waveform corresponding to the Tolbachik eruption (the cross-correlation on January 20, 2013 shown with the blue colour in (b) and indicated with the blue arrow). (e) Matrix of correlation coefficients between all daily cross-correlation waveforms for the station pair CIR-LGN. Eruption time intervals of Klychevskoy and Tolbachik volcanoes are indicated with horizontal red lines in (c) and (d).

6 Network-based analysis of seismic tremor wavefields

When a seismo-volcanic tremor is recorded by multiple stations of a network, the ensemble of inter-station cross-correlations provides us with a very convenient representation of the wavefield. This ensemble forms a network cross-correlation matrix (including auto-correlations) in the time domain and its equivalent in the spectral domain is the cross-spectral or covariance matrix. Therefore, in this section we will introduce the "network covariance matrix" - a mathematical object that is central in most of methods of network- or array-based signal analysis aimed at detection, separation, and location of seismic sources. In this section, we will consider some of these methods that are pertinent for the analysis of seismic tremors. At the same time, the network-based analysis is a very large field and the description presented in this section is not either complete or unique. Many methods or their variants are not considered here. Also, some

methods described here (e.g., beamforming, back-projection) can be formulated in many different ways. The interested readers can find more details about the network-based analysis in specialized textbooks, web-sites, and scientific papers (some of which are included in the reference list).

6.1 Definition of the network covariance matrix

In the following analysis we use conventions from Seydoux et al. (2016) and consider only vertical component records. Let's consider the network data vector $\mathbf{u}(t) = [u_1(t)\, u_2(t)\, \ldots\, u_N(t)]^T$, where $u_i(t)$ is the seismic trace registered by the seismometer i, N is the number of sensors and T denotes the transpose operator. Its Fourier transform in the frequency domain is $\mathbf{u}(f) = [u_1(f)\, u_2(f)\, \ldots\, u_N(f)]^T$. From a mathematical point of view, the network covariance matrix $\mathbf{C}(f)$ is defined as the expected value of the cross-spectra product between $\mathbf{u}(f)$ and its transposed complex conjugate :

$$\mathbf{C}(f) = \mathbf{E}\left[\mathbf{u}(f)\, \mathbf{u}^{\dagger}(f)\right] \tag{12}$$

where $\mathbf{E}$ stands for the Expected Value and † denotes the Hermitian transpose (complex conjugate transpose). The network covariance matrix is inherently Hermitian and positive semidefinite. Therefore, it is diagonalizable and can be decomposed on the basis of its complex eigenvectors associated with real positive eigenvalues.

When working with real data, the estimation of the network covariance matrix requires several steps. First, the used seismic records must be pre-processed to enhance certain types of signals that are targeted in the analysis and to diminish a possible influence of "non-desired" signals, as detailed in section 6.2. In a second step, inter-station covariances of pre-processed records are statistically estimated as described in section 6.3.

6.2 Pre-processing of seismograms

Standard preparation of the digital seismograms for the network-based analysis generally includes: instrument correction (preceded by both detrending and tapering), decimation (to reduce the data volumes and the amount of computations), sample alignment, managing the data gaps and overlaps, and organizing the records in segments of proper lengths.

Then, a specific pre-processing aimed at analyzing volcanic tremors is needed. Because of the continuous nature of the tremor signals, the pre-processing used for their analysis is very similar to the case of seismic noise (Bensen et al., 2007). It may start with filtering signals in the frequency bands corresponding to tremors. Then, the amplitudes could be normalized in both time and spectral domains. The time domain normalization is important to diminish the influence of earthquakes and other strong impulsive signals in order to emphasize the network-wide coherence of the wavefield formed by long-duration tremors. At the same time, for some types of intermittent tremors the amplitude modulation might be a very distinctive and important feature. In this latter case, the amplitude normalization in time might be omitted (Soubestre et al., 2018). The spectral domain normalization is important to compensate for the dominance of most intense spectral peaks that are often present in tremors (Chouet, 1996). Without normalization, these peaks might be strongly amplified in the covariances where the spectral amplitude is squared (equation 9).

Spectral whitening consists in dividing the signal spectrum by a smooth version of its amplitude:

$$u^W(f) = \frac{u(f)}{\langle\langle |u(f)| \rangle\rangle_{df}} \tag{13}$$

where $|u(f)|$ represents the real absolute value of the spectrum, and $\langle\langle \cdot \rangle\rangle_{df}$ stands for the smoothing in the frequency domain with a running window of a df length. The normalization is done similarly in the time domain:

$$u^N(t) = \frac{u^W(t)}{\langle\langle |u^W(t)| \rangle\rangle_{dt}} \tag{14}$$

where $u^W(t)$ is the real part of the inverse Fourier transform of $u^W(f)$, and $\langle\langle \cdot \rangle\rangle_{dt}$ is the smoothing in the time domain with a running window of a dt length. If no smoothing is applied ($df, dt = 0$), the amplitude information in the initial data is completely ignored.

6.3 Estimation of the network covariance matrix

We estimate the covariance matrix $\mathbf{C}(f)$ from the time average of the Fourier cross-spectra matrices computed over a set of M overlapping subwindows of length δt (see Figure 8). Filtered and decimated traces form the network data vector of one-component (vertical or horizontal) data $\mathbf{u}(t) = [u_1(t)\ u_2(t)\ ...\ u_N(t)]^T$, where t is the time, $u_i(t)$ is the trace at station $i = 1, ..., N$ and N is the number of sensors composing the network. The data vector is subdivided into overlapping time windows (generally with 50% of overlap), within which amplitudes are normalized (independently for each station). Every pre-processed window starting at a specific time t is then subdivided into M overlapping subwindows (generally with 50% of overlap) of duration δ_t, on which $\hat{\mathbf{u}}_m(f, t + m\delta_t/2)\, \hat{\mathbf{u}}_m^\dagger(f, t + m\delta_t/2)$ cross-spectra matrices are computed, where $m = 0, ..., M-1$; $\dagger$ denotes the Hermitian transpose (complex conjugate transpose); and $\hat{\mathbf{u}}_m(f, t+m\delta_t/2)$ is the Fourier transform of the pre-processed data vector $\mathbf{u}_m(t+m\delta_t/2)$. A network covariance matrix $\mathbf{C}$ is then estimated on each pre-processed window starting at time t and with duration $\Delta_t = r(1 + M)\delta_t$. This estimation corresponds to an average of the cross-spectra matrices computed on the M overlapping subwindows:

$$\mathbf{C}(f,t) = \frac{1}{M} \sum_{m=0}^{M-1} \hat{\mathbf{u}}_m(f, t + m\delta_t/2)\, \hat{\mathbf{u}}_m^\dagger(f, t + m\delta_t/2) \tag{15}$$

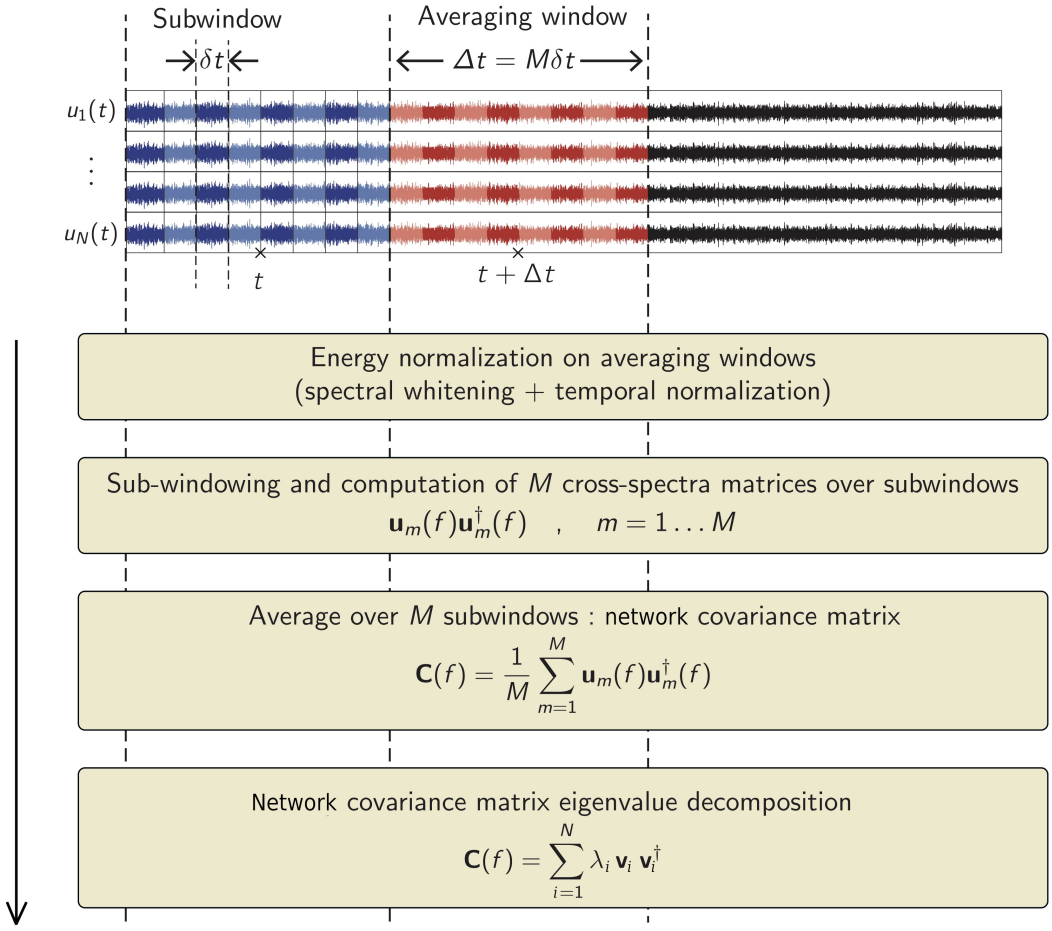

Figure 8: **Sequence of operations used for estimating the network covariance matrix from continuous seismic records.** Modified from Seydoux et al. (2016).

It is important to remember that the estimation of the network covariance matrix with equation (15) is strongly non-unique and depends both on the pre-processing of the raw data and on the parameters used in the averaging (number M and length δ_t of subwindows). Depending on the nature of the targeted signals, the choice of these parameters can be very different. For continuous and near-stationary tremors, a pre-processing removing the influence of amplitudes together with large number of long time windows might be used. On the contrary, for shorter signals, keeping the amplitude information and using shorter averaging time might be necessary.

The network covariance matrix (15) being inherently Hermitian and positive semidefinite (Seydoux et al., 2016), it can be decomposed on the basis of its complex eigenvectors $\mathbf{V}_i$ associated with real positive eigenvalues λ_i:

$$\mathbf{C}(f,t) = \sum_{i=1}^{N} \lambda_i(f,t)\mathbf{V}_i(f,t)\mathbf{V}_i^{\dagger}(f,t) \tag{16}$$

In the following paragraphs we will discuss how the network covariance matrix can be used for small-aperture array analysis (6.4), while the distribution of its eigenvalues can be used for tremor detection (6.5), whereas the first eigenvector can be used for separating (6.6) and locating (6.7) different tremor sources.

6.4 Beamforming of volcanic tremor with small-aperture arrays

A seismic array is a group of seismic stations with inter-station distances being smaller than a half-wavelength of the studied signal. Indeed, when measuring a propagating waveform of a seismic signal using an array, its configuration and sensors spacing define a spatial sampling rate, which has to be higher than half of the considered signal wavelength in order to avoid spatial aliasing. Such spatial aliasing thus occurs when the seismic wavefield spatial variations are not well resolved by the array, leading to distortions and inaccuracies in the estimated locations and characteristics of the tremor sources. In volcanoes, a seismic array generally contains between five and a few tens of seismometers. The array aperture is typically a few hundreds of meters, with interstation distances of a few tens of meters. We note that the array aperture defines its resolution for small wavenumbers and it should be larger than the largest considered wavelength so that the corresponding seismic signal can be meaningfully analyzed (Schweitzer et al., 2012).

One advantage of arrays compared to single station analysis is the improvement of the signal-to-noise ratio (SNR) thanks to the summation of individual recordings of the array stations (Rost and Thomas, 2002). More importantly, arrays can be used for beamforming providing knowledge about the direction of propagation of tremor waves (azimuth) and their velocity (or its inverse, the slowness). These parameters can then be used to determine the source location, especially by combining results from multiple arrays.

The array analysis is based on the assumption that the source is located outside of the array and at a distance exceeding its aperture. In this case, the incoming wavefield can be approximated as a plane wave described by a slowness vector $\mathbf{p}$, or by its absolute value p and azimuth θ. Then, the differential travel times δt_{ij} between array elements i and j are related to their respective known positions $\mathbf{r} = (x, y)$ by the following equation:

$$\delta t_{ij} = \mathbf{p}\ \ (\mathbf{r}_i - \mathbf{r}_j) = p\ [(x_i - x_j)\cos\theta + (y_i - y_j)\sin\theta] \tag{17}$$

If the ensemble of inter-station travel times is measured, for example from the "ballistic" part of the inter-station cross-correlations (11), equation (17) can be used to estimate the azimuth and the slowness of the incoming wave. However, measuring these travel times with a visual analysis of cross-correlation waveforms might be not simple because of their complexity (see Figure 6) and not practical for an extensive analysis of continuous data. Therefore, the practical implementation of the array analysis is often based on the plane-wave beamforming, that is aimed to estimate the parameters of the slowness vector directly from the continuous records (or their covariances) and whose basic mathematical expression can be derived by projecting the covariance matrix (15) on the functional sub-space formed by plane wave replicas:

$$\mathbf{b}(f,p,\theta) = \exp(2i\pi f p[\mathbf{x}\cos\theta + \mathbf{y}\sin\theta]) \tag{18}$$

where f is the frequency, and $\mathbf{x}$ and $\mathbf{y}$ are the vector of coordinates of the array sensors. The beamforming $\mathbf{B}(f,t,p,\theta)$ is then defined as:

$$\mathbf{B}(f,t,p,\theta) = \mathbf{b}^{\dagger}(f,p,\theta)\ \mathbf{C}(f,t)\ \mathbf{b}(f,p,\theta) \tag{19}$$

The retrieved distribution of energy on the slowness-azimuth plane can be used both for detection of tremors and for estimating the parameters of the slowness vector at its maximum. The basic idea of many detectors is to identify whether a clear peak corresponding to a tremor source is present or not in $\mathbf{B}(f,t,p,\theta)$. It is important to mention that equations (18) and (19) present only one version of the plane-wave beamforming while many others not considered here exist (see Rost and Thomas, 2002, for a review of beamforming methods).

In order to evaluate the sensitivity and resolution of an array for seismic signals with different frequency contents and slowness, the array response function (ARF) is defined such as the beampower for a given plane-wave model, array configuration and beamforming method (Schweitzer et al., 2012; Ruigrok et al., 2017). The ARF quantifies how seismic waves arriving at different sensors are combined and weighted, and it can be computed prior to the actual array installation to assess and optimize the detection, localization and characterization of seismic sources.

It is also possible to use other replicas than plane wave replicas. In particular, when sources are located within or in the vicinity of an array, spherical or cylindrical replicas can be used. A more advanced version is to use replicas based on travel times predicted in a heterogeneous medium model. All this gives rise to a family of methods known as matched field processing (e.g., Baggeroer et al., 1988; Kuperman and Turek, 1997; Almendros et al., 1999; Nanni et al., 2021).

Different versions of the beamforming with small arrays have been used to track the sources (or more exactly the back-azimuth and the apparent slowness of the recorded wavefield) of tremors and other types of seismicity in different volcanoes. Almendros et al. (1997) studied the time evolution of both volcanic tremor and hybrid events at Deception Island, Antarctica. The tremor was found to be composed of overlapping hybrid events. Highly coherent harmonic tremor was also studied by Almendros et al. (2014) at Arenal volcano. It was characterized by stable apparent slowness vector estimates, with backazimuths generally pointing towards the volcano. Furumoto et al. (1990, 1992) located the source of tremor at Izu-Oshima volcano, Japan. Tremor sources composed of discrete pulses were located at Mt Etna (Seidl et al., 1981), Stromboli (Chouet et al., 1999), Mt Aso (Kawakatsu et al., 1994, 2000), Mt Erebus (Rowe et al., 2000) and Iwate (Nishimura et al., 2000). Seismic surface waves coming from the crater of a volcano were associated with a shallow tremor source at Kilauea (Ferrazzini et al., 1991; Saccorotti et al., 2003), Masaya (Métaxian et al., 1997), and Stromboli (Chouet et al., 1998). The array analysis enabled to identify three co-eruptive tremor sources associated with opening of new vents, growing margins of the lava field and intrusions during the 2014-2015 Holuhraun eruption in Iceland (Eibl et al., 2017a). It was also used to study shallow tremor close or beneath beneath Puu Oo crater (Goldstein and Chouet, 1994) and Halemaumau crater (Almendros et al., 2001) at Kilauea volcano, Hawaii.

The intersection of backazimuth directions obtained at different arrays provides a joint location of the tremor source in the horizontal plane (2-D location). This technique has been used with different number of arrays. *Two arrays* were used to locate shallow tremor beneath Puu Oo crater at Kilauea volcano (Goldstein and Chouet, 1994), shallow permanent tremor at Masaya volcano (Métaxian et al., 1997), volcanic tremor preceding and accompanying the 2004-2005 eruption of Etna volcano (Di Lieto et al., 2007), and tremor related to sub-glacial floods from draining glacier-dammed lakes in Skafta cauldrons at Vatnajökull glacier, Iceland (Eibl et al., 2020). A tremor source was located with *three arrays* close to Halemaumau crater at Kilauea volcano (Almendros et al., 2001). Finally, a tremor location centered on the active crater was obtained with *four arrays* at Arenal (Métaxian et al., 2002). Once the 2-D location obtained, the tremor source depth can be estimated if a 1-D velocity model is available (Almendros et al., 2001).

Smith and Bean (2020) recently provided a python-based software called RETREAT that uses seismic array data and array processing techniques to compute backazimuth and slowness in near-real time in order to improve tremor sources tracking and monitoring capabilities.

6.5 Detection of tremor based on distribution of eigenvalues of the network covariance matrix

The small aperture arrays described in previous paragraphs can be installed during dedicated (and often relatively short-duration) field experiments. Maintaining such dense arrays for the routine continuous monitoring of volcanoes is not practical. Seismic monitoring networks operated by volcano observatories are rather extended over relatively large territories to cover different possible sources of seismicity. As a result, inter-station distances are much larger than wavelengths and, more importantly, most of tremor sources are located inside the networks. With such configuration, the plane-wave beamforming cannot be used and other methods need to be applied.

A first idea is to use the distribution of eigenvalues of the covariance matrix expressed as equation (16). It can be argued (e.g., Gerstoft et al., 2012; Seydoux et al., 2016), that if a wavefield is generated by a single source, the rank of the resulting covariance matrix will be equal to one. For K spatially separated and statistically independent sources, the matrix will be of rank K. This implies that the rank of the covariance matrix could be used as a proxy for the number of sources. However, using the rank of the covariance matrix is not practical because in the presence of noise it will be always non-zero. Therefore, the distribution of eigenvalues must be analysed in order to determine if one (or a few) of them

dominates, which would be the case of one (or a small number of) tremor source, or if the distribution is rather "flat", which would be the case of noise excited by many incoherent sources.

Based on these arguments, a scalar parameter $\sigma(f,t)$ called "spectral width" introduced by Seydoux et al. (2016) and defined as the width of the distribution of eigenvalues (with eigenvalues sorted in decreasing order) can be used to automatically detect tremor:

$$\sigma(f,t) = \frac{\sum_{i=1}^{N}(i-1)\lambda_i(f,t)}{\sum_{i=1}^{N}\lambda_i(f,t)} \tag{20}$$

This spectral width may be viewed as a proxy for the number of independent seismic sources composing the wavefield. Thus, the spectral width corresponding to ambient seismic noise composed of uncorrelated signals (with random phases) produced by spatially distributed noise sources would be relatively large. Conversely, the spectral width of a signal generated by a single localized source would be small.

The time-frequency-dependent spectral width $\sigma(f,t)$ computed from four and a half years of data (from January 2009 to May 2013) recorded by a network composed of 19 stations deployed at the Klyuchevskoy Volcanic Group in Kamchatka is shown in Figure 9. Each pixel of this time-frequency plot represents the spectral width at a given time and frequency. This plot obtained from a network-based approach is therefore distinct from a spectrogram, which is related to the signal amplitude at an individual station and might be strongly affected by site effect. Spatially coherent signals (in terms of phase) of the wavefield appear with low spectral width value (red color) in Figure 9, and periods dominated by uncorrelated noise appear with high spectral width value (blue color). Thus, the two months-long signals detected in the frequency range 0.4-3.0 Hz in 2009-2010 and 2012-2013 correspond to volcanic tremor (more details can be found in Soubestre et al. (2018)).

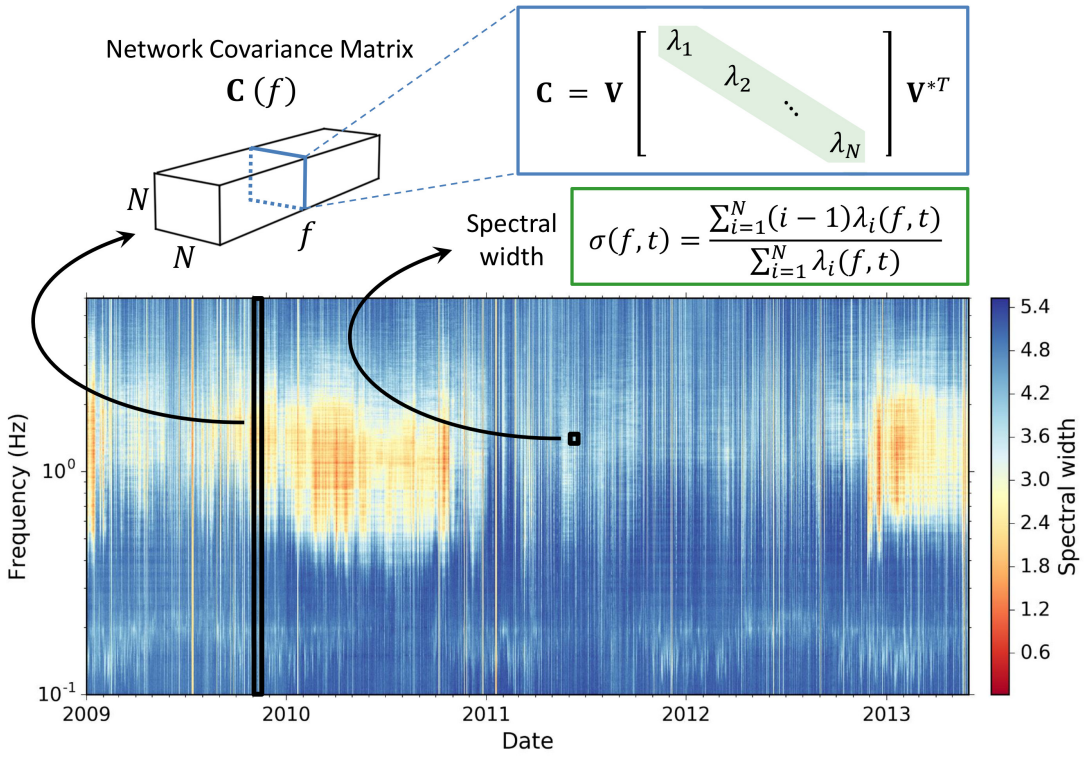

Figure 9: **Detection of tremors at KVG with the network covariance matrix method**. Modified from Soubestre et al. (2018). Time-frequency-dependent spectral width computed from four and a half years of data recorded by a network composed of 19 stations deployed at the Klyuchevskoy Volcanic Group in Kamchatka. It is computed with the following parameters explained in section 6.3: time windows of length $\Delta_t = 25,000$ s composed of $M = 50$ subwindows of length $\delta_t = 1,000$ s overlapping at 50 %. The network covariance matrix and the spectral width corresponding to a time window and a pixel of the plot, respectively, are shown on top of it. The two months-long signals detected in the frequency range 0.4-3.0 Hz in 2009-2010 and 2012-2013 correspond to volcanic tremor from Klyuchevskoy and Tolbachik volcanoes, respectively, as inferred from *a priori* knowledge (Droznin et al., 2015).

The spectral width is a very efficient and robust detector of tremors and does not depend on any

assumption about the source location and type of emitted waves (as it must be done in the case of beamforming). At the same time, this simple scalar parameter is not sufficient to distinguish different tremor sources. In the particular case of KVG, it is not possible to know whether the 2009-2010 and 2012-2013 tremors detected in Figure 9 correspond to the same tremor source at a given volcano activated at different periods, or to different sources at a single or multiple volcanoes. In the present case, the association of 2009-2010 and 2012-2013 tremors to Klyuchevskoy and Tolbachik volcanoes, respectively, is inferred from *a priori* knowledge (Droznin et al., 2015). But for this distinction to be automatically integrated into the network covariance matrix analysis, it is necessary to analyze the eigenvectors of the covariance matrix and particularly the first eigenvector, as detailed in sections 6.6 and 6.7.

6.6 Distinguishing between different sources of tremor

As discussed in section 5, inter-station cross-correlations contain a rich information that can be used to distinguish different sources of seismic tremor not only based on their spectral content but more importantly based on signatures of the seismic wave propagation from different locations that are contained in the phase of the cross-correlation waveforms (or cross-spectra). The eigenvalue-based analysis described in previous paragraphs ignores this phase information that is contained in the eigenvectors of the network covariance matrix expressed as equation (16). Here we use the first eigenvector $\mathbf{V}_1(f,t)$ that characterizes the dominant source of the seismic tremor as a "fingerprint". This can be considered as an extension of the approach based on a single-pair cross-correlation (section 5) to a whole network.

Eigenvectors of the matrix (16) are complex and defined in the spectral domain. Therefore, to characterize their level of similarity, we introduce a correlation coefficient $cc_{k,l}(f)$ between the first eigenvectors from windows k and l : $\mathbf{V}_1(f,t_k)$ and $\mathbf{V}_1(f,t_l)$. These vectors being complex, the correlation coefficient is defined at each frequency as the absolute value of the complex scalar product normalized by the respective norms:

$$cc_{k,l}(f) = \frac{|\mathbf{V}_1(f,t_k)\mathbf{V}_1^*(f,t_l)|}{\|\mathbf{V}_1(f,t_k)\|\,\|\mathbf{V}_1(f,t_l)\|} \tag{21}$$

Then, an average correlation coefficient $\overline{cc}_{k,l}$ is computed as the mean of the n_f correlation coefficients calculated in a selected frequency band between f_1 and f_2:

$$\overline{cc}_{k,l} = \frac{1}{n_f}\sum_{f_1}^{f_2} cc_{k,l}(f) \tag{22}$$

An ensemble of such average correlation coefficient computed between all time windows forms a matrix. An example of such matrix computed from the KVG monitoring seismic network during 2009-2013 is shown in Figure 10a. In this case, day-long inter-station cross-correlations have been used and the correlation coefficient has been averaged between 1 and 2 Hz. This matrix has a structure that reveals several periods of elevated similarity between distinct days, implying that the dominating tremor source remained stable during those periods. It resembles the one based on just one pair of stations (Figure 7e) but with some clusters of activity being better isolated because of using all possible station pairs.

Different sources of tremor can be identified from matrix (22), for example, with a similarity-based clustering algorithm described in Soubestre et al. (2018). It works in two steps: 1) selection of initial clusters and 2) iterating and resorting to obtain the final clusters.

The first step contains three stages. First, correlation coefficients $\overline{cc}_{k,l}$ are averaged in time in a moving window. The window duration might be selected as approximately equal to the lower limit of duration of considered tremor episodes. In the case of KVG, we used a 20-day-long window, thus aimed at rather long continuous tremors. When analysing intermittent tremors (e.g., Fujita, 2008; Cannata et al., 2010), a shorter window might be more adequate. A result of this operation is shown with a black line in panel 2 of Figure 10a. The maximum of this averaged correlation coefficient determines the initial cluster central window (vertical red line in panel 2, Figure 10a), called centroid. Second, the line (or column) of the average correlation coefficients matrix corresponding to this centroid is considered (black line in panel 3, Figure 10a) and only the windows with a correlation higher than a given threshold s_{cc} (red line in panel 3, Figure 10a) are kept in the cluster (green rectangles in panel 3, Figure 10a). Third, windows corresponding to this cluster are removed from the matrix (panel 4, Figure 10a) and the process is continued iteratively up to the determination of the n_{clus} initial clusters.

The second step consists in resorting the initial clusters. It is realized in an iterative way. Each iteration of resorting contains two stages. First, the centroid of each of the n_{clus} initial clusters is redefined by time stacking the coefficients $\overline{cc}_{k,l}$ not anymore through a n_{days}-long moving window, but

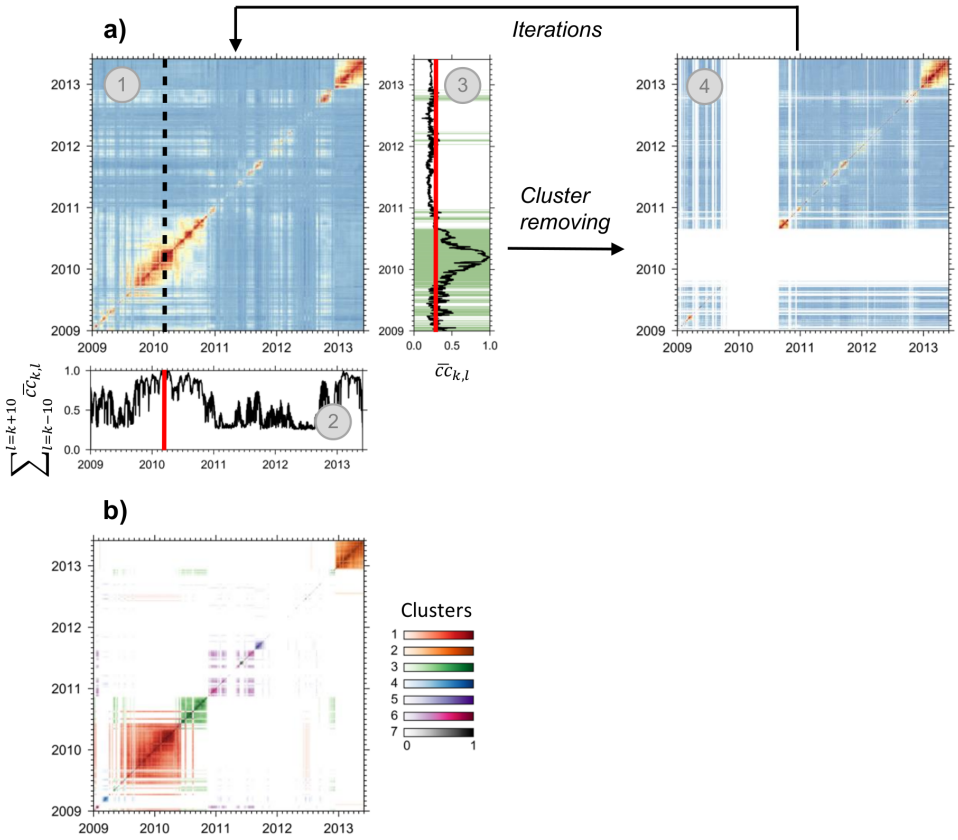

Figure 10: **Clustering of tremors at KVG with the network covariance matrix method**. Modified from Soubestre et al. (2018). (a) Iterative procedure of identification of clusters, as detailed in section 6.6. (a-1) Matrix of correlation coefficients computed between dominant eigenvector (equation 22). One-day-long time windows and 1-3 Hz spectral band have been used. (a-2) Finding a centroid of the first cluster. (a-3) Selecting days with similar first eigenvectors. (a-4) Removing the first cluster from the matrix. (b) Time-time representation of the final seven clusters associated with tremor activity at four different volcanoes based either on *a priori* knowledge or on locating tremor sources (section 6.7). Color scales correspond to correlation coefficient relative to the cluster centroid.

through a window containing only the days of the concerned cluster determined in the first step. Second, each day of the studied period (from January 2009 to May 2013 in the case shown in Figure 10) is compared to those n_{clus} redefined centroids (second step, first stage) and placed in the cluster where the correlation is the highest. With the parameters $n_{clus} = 10$, $n_{days} = 20$ and $s_{cc} = 0.3$ used in the example shown in Figure 10a, it takes three iterations for the iterative process to converge, i.e. for the redefined centroids to not change between two consecutive iterations.

Note that once the window duration n_{days} fixed, the clustering result is not very sensitive to the values of parameters s_{cc} and n_{clus}. The latter just needs to be higher than the potential number of distinct tremor sources. Here $n_{clus} = 10$ is adapted to the case of KVG with several erupting volcanoes and episodes of activity, but a smaller value could be used in less active volcanic systems.

Figure 10b shows the first seven clusters associated with tremor activity (the remaining three clusters are associated with noise). In addition to the two tremor episodes in 2009-2010 and 2012-2013 already detected by the spectral width approach in Figure 9, other time periods related to tremor activity are highlighted by the clustering approach, in particular in 2011. Based on *a priori* knowledge, four volcanoes were active during the 2009-2013 studied period, namely Klyuchevskoy, Tolbachik, Shiveluch and Kizimen. The seven clusters are therefore associated with the activity at those four volcanoes. Given that a specific tremor source is supposed to be associated with each cluster, different clusters are necessarily associated with a single volcano. Possible explanation of this is either that the tremor-generating activity migrated or that the tremor-generating process changed. In particular, additional analysis show that clusters 1 and 3 of Figure 10b are associated with noneruptive tremor and eruptive tremor at Klyuchevskoy, respectively (Soubestre et al., 2018). Note that being based on the scalar parameter $\overline{cc}_{k,l}$ removing the space information and containing only the time dimension (cf. equations

(21) and (22)), the clustering approach described here is able to distinguish tremor sources in time but not in space. For the distinction in both time and space to be automatic and integrated to the network covariance matrix analysis, it requires to keep the spatial information contained in the first eigenvector, as in the location approach detailed in the following sections.

6.7 Covariance-based location of tremor sources

Methods of volcanic tremor sources location from network cross-correlations have been proposed in different studies (e.g., Ballmer et al., 2013; Droznin et al., 2015; Soubestre et al., 2019; Li and Gudmundsson, 2020). The common idea is to use the differential travel times contained in inter-station cross-correlations (equation 11) in order to "back-project" the tremor signals energy toward its source. Often, tremor sources are considered as *a priori* shallow and cross-correlations are assumed to be dominated by surface waves. This assumption leads to a 2-D location scheme. However, in many cases tremor sources are located at significant depths (more than a few km) and in this case a 3-D back-projection based on a body-wave (most often S-wave) assumption must be implemented. The network covariance matrix formalism also allows to better isolate contribution from the dominant tremor source via selecting the first eigenvector which leads to a slightly more accurate location (Soubestre et al., 2019). An important limitation of the location method presented in this section is the assumption of a single dominating source leading to a single dominant eigenvalue/eigenvector. In the case of multiple simultaneously acting sources, a more advanced approach should be developed with analyzing several eigenvectors in order to separate the different sources.

The filtered covariance matrix $\tilde{\mathbf{C}}(f,t)$ is extracted from equation (16) by computing the complex outer product of the first eigenvector $\mathbf{v}^{(1)}(f,t)$ with its Hermitian transpose:

$$\tilde{\mathbf{C}}(f,t) = \mathbf{v}^{(1)}(f,t)\,\mathbf{v}^{(1)\dagger}(f,t) \tag{23}$$

This operation can be seen as a low-rank denoising of the covariance matrix, a strategy widely used in image processing to remove the noise spanned by higher-order eigenvectors (Orchard et al., 2008). The inverse Fourier transform of this matrix retrieves the time-domain filtered cross-correlations:

$$\tilde{\mathbf{CC}}(\tau,t) = \mathcal{F}^{-1}\tilde{\mathbf{C}}(f,t) \tag{24}$$

where $\mathcal{F}^{-1}$ is the inverse Fourier transform operated to the frequency dimension, and τ is the cross-correlation lag-time. Non-diagonal elements of this matrix $\tilde{CC}_{i,j}(\tau,t)$ are the "filtered" inter-station cross-correlations.

These cross-correlations are then "back-projected" to find the tremor source position. This back-projection is realized as a grid search in a 3-D space. First, all points of the grid $\mathbf{r}$ are considered as potential sources, and travel times $\tau_i(\mathbf{r})$ to all stations (i) of the network are predicted based on a known velocity model of the sub-volcanic medium. In most cases tremors are considered to be dominated by S-waves. Ideally, 3-D velocity models can be considered. However, in most volcanic areas, these are not accurate enough and average 1D velocity models lead to more robust location results. The smoothed amplitude envelopes $E_{i,j}(\tau,t)$ of $\tilde{CC}_{i,j}(\tau,t)$ are then computed and shifted with respect to differential travel times:

$$d\tau_{ij}(\mathbf{r}) = \tau_i(\mathbf{r}) - \tau_j(\mathbf{r}) \tag{25}$$

Finally, a network response function R is estimated as the value at zero lag-time of the sum of smoothed and shifted envelopes for all stations pairs:

$$R(\mathbf{r},t) = \sum_{i=1}^{N}\sum_{j>i}^{N} E_{ij}(\tau - d\tau_{ij}(\mathbf{r}),t)\Big|_{\tau=0} \tag{26}$$

This version of back-projection does not involve a coherent summation of cross-correlation waveforms but of their smoothed amplitude envelopes. This reduces the alteration of the location quality from scattering due to local heterogeneities and from the imprecision of the location method itself, particularly the imprecision of the velocity model. Finally, the function $R(\mathbf{r},t)$ can be interpreted as a spatial likelihood of the tremor source location and the most probable source position can be defined at its maximum. Examples of tremor sources located at KVG are shown in Figure 11.

Tremor location error can be estimated by measuring the spatial distribution of high values of the spatial likelihood function above a certain threshold. For the Kamchatka tremor sources, this measurement shows an increase in vertical error from a few kilometers near the surface, to around 10 km towards

30 km depth (Journeau et al., 2022). In addition, it can be useful to measure the distance between the hypocenter of an earthquake located using the P and S wave arrival times and the coordinates of the maximum of the spatial likelihood function calculated for a time window containing this earthquake. Permana et al. (2019) show that the resulting misfit is around 2 km or less using VT hypocenters below the Izu-Oshima volcano. This average misfit is about 7 km for DLP earthquakes located around 30 km below the Klyuchevskoy volcano (Journeau et al., 2022).

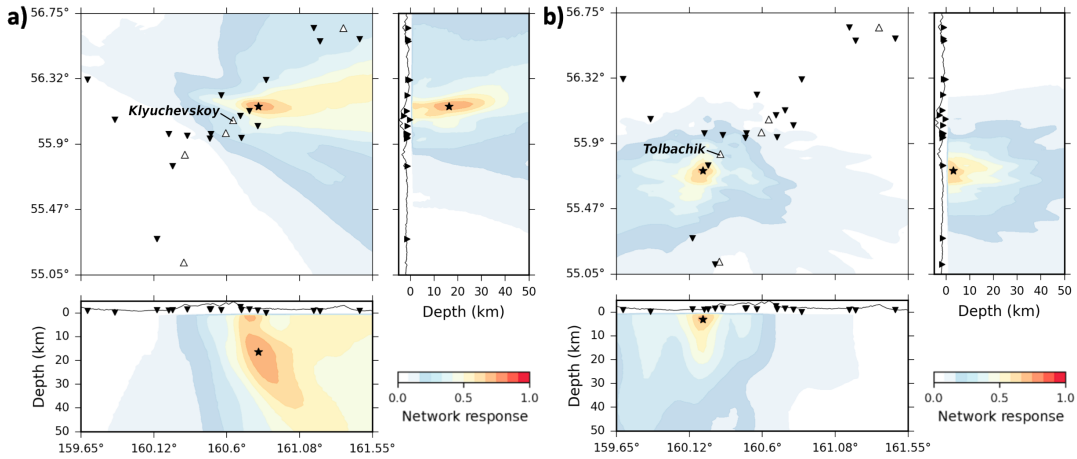

Figure 11: **Location of tremor sources at KVG with the network covariance matrix method**. Modified from Soubestre et al. (2019). Colored contours show tremor source presence likelihood (equation (26) with envelopes smoothed in a 10-day-long window). The most probable tremor source location is marked by a black star. Seismic stations and volcanoes respectively appear as black inverted triangles and white triangles in the horizontal top view (center panel). (a) Deep tremor beneath Klyuchevskoy on October 3, 2009. (b) Shallow tremor beneath Tolbachik on March 4, 2013.

7 Application examples

In addition to examples shown in previous sections, we illustrate the network-based analysis of seismic tremor with two studies of very active and well-instrumented volcanic systems. The first example is the 2018 Lower East Rift Zone eruption of Kilauea Volcano, Hawaii, that generated multiple sources of rather shallow tremor at the summit region in the Kilauea Caldera. The second example is from the Klyuchevskoy Group of Volcanoes in Kamchatka, Russia, where a large regional-scale network has been installed during 2015-2016 and recorded seismic tremors originating beneath different active volcanoes over a large range of depths from the crust-mantle boundary to the surface. In both cases, we discuss how the network-based analysis can be used to distinguish different sources of tremor and to test possible hypotheses about their origin.

7.1 Shallow seismic tremor at Kilauea volcano, Hawaii

The present section describes an example of analysis of several shallow volcanic tremor sequences which accompanied the summit activity during the 2018 Lower East Rift Zone eruption of Kilauea Volcano, Hawaii. More details about this case study can be found in Soubestre et al. (2021). The eruption was marked by a dyke intrusion and the production of voluminous lava flows in the lower east rift. Magma withdrawal from the summit region induced summit subsidence and triggered the draining of an active lava lake in the Halemaumau Crater in the Kilauea Caldera. The surface of the lava lake started to drop on May 2, 2018 (Neal et al., 2018), synchronous with the onset of the summit steady subsidence associated with elastic decompression (Anderson et al., 2019). Over the intervening week the lava lake dropped more than 300 m, eventually vanishing from sight on May 10, 2018 (Neal et al., 2018). Sustained magma withdrawal induced a drop of the floor of Halemaumau, which progressed in a series of 12 rapid semi-regular collapses corresponding to inelastic failures starting on May 17, 2018. As the eruption continued over the next three months, surface collapse grew beyond Halemaumau to encompass large portions of the caldera to the east and west. A total of 62 collapse events occurred in the caldera up to early August when the summit subsidence and the emission of lava in the lower east rift essentially

ceased. By August 2, 2018, the collapses had resulted in 5 km^2 of the caldera dropping between 120−470 m.

Volcanic tremor exhibited strong changes relative to the dynamic behavior at the summit of Kilauea as it evolved from steady state activity through April, to elastic subsidence in early May, and inelastic collapses from mid-May onward (Anderson et al., 2019). The time-frequency-dependent spectral width $\sigma(f,t)$ computed from two months of data (from April 15 to June 15, 2018) recorded by a network composed of 12 broadband seismic stations deployed at the summit with an aperture of 5 km (Figure 12e) is shown in Figure 12a. The time series of a tiltmeter co-located with one of the seismometers on the northwest flank of Kilauea Caldera (station UWE, Figure 12e) is shown as a black line superimposed on the spectral width plot. Distinct tremor sources identified in this figure are described below and discussed in more detail in Soubestre et al. (2021). The tremor sources are located with the method described in section 6.7, on a 3-D grid covering the 8.4 km × 6.6 km summit region shown in Figures 12b-d down to 6 km depth, with a 200 m resolution in both horizontal and vertical directions. Note that the low spectral width saturation clearly visible in the 0.1–0.3 Hz frequency band in Figure 12a corresponds to some spatial aliasing due to the network size and prevents the oceanic microseismic noise from being correctly detected (Soubestre et al., 2021).

Two very-long-period tremors are clearly detected in Figure 12a at frequencies near 0.026−0.027 Hz (periods 37−38 s) and 0.060−0.070 Hz (periods 14−17 s). Those tremors are stable before May 5 and vanish during the period when the magma withdraws and the lava lake drops out of sight (May 10), evidencing their direct relation with the lava lake itself. Note that owing to the very long wavelength of those signals (on the scale of one hundred kilometers) compared to source-station distances (a few kilometers), the cross-correlation based location method described in section 6.7 cannot be applied to locate their sources, because at such very low frequency all cross-correlations of the considered network turn to auto-correlations. Nevertheless, the 0.026−0.027 Hz and 0.060−0.070 Hz tremors have been well characterized in different studies and correspond to the breathing mode of the lava lake mass perched on top of a dual dyke plexus (Chouet et al., 2010; Chouet and Dawson, 2011) and to sloshing modes of the lava lake (Dawson and Chouet, 2014), respectively.

A stable long-period tremor is present in Figure 12a in the frequency range 0.5−1.0 Hz before May 5 (green box, Figure 12a). Source locations of this tremor for consecutive 6 hour-long time windows point to a surficial source positioned at the south-southwest edge of the Halemaumau Crater (green dots, Figure 12b). The source is bracketed by the east-striking and north-striking dykes in the dual dyke system imaged by Chouet and Dawson (2011) (red and blue dashed lines, respectively, Figure 12e), where it sits approximately 200 m south of the surface trace of the east dyke and 500 m west of the surface trace of the north dyke. The proximity of these spatially extended heat sources, together with the presence of abundant meteoritic water in the caldera and the surficial character of this activity, are strongly suggestive of a hydrothermal origin. This tremor is therefore attributed to the quasi-steady radiation from a shallow hydrothermal system positioned at the south-southwest edge of Halemaumau Crater.

Two sequences of gliding tremor appear in the frequency range 0.3−3.0 Hz in Figure 12a. The first sequence of gliding tremor occurs between May 7 and May 16 (orange box, Figure 12a), when the magma withdraws and the lava lake disappears (May 10). The second sequence occurs between May 17 and May 27 (red box, Figure 12a), when the first 12 collapses occurred in Halemaumau Crater. A different interpretation of those two gliding tremors is sustained by four arguments: distinct continuous and discrete nature of the glidings, distinct surface activity observed during the two sequences, distinct spatial locations of the tremor sources, and distinct ratios of excited frequencies implying different physical models of their source processes.

The first sequence of continuous gliding tremor occurs between May 7 and May 16, just after the shallow hydrothermal system associated with the 0.5−1.0 Hz long-period tremor ceased its steady state activity and before the start of the 12 collapses that affected the Halemaumau Crater. Sources of this gliding tremor are located near the northwest, west, southwest, and south edges of Halemaumau Crater (orange dots, Figure 12c). This gliding tremor is attributed to the progressive intrusion of a rock piston into the leaky hydrothermal system (following Kumagai et al. (2001) who modeled VLP signals associated with the caldera formation at Miyake Island with a rock piston intruding into the leaky magma chamber). This interpretation is supported by topographic images showing that the region west and southwest of Halemaumau was the first region outside of the crater to collapse in early June (orange circle, Figure 12e), evidencing the potential weakening of this zone due to the presence of the hydrothermal system. It is further supported by the observation that most ejecta in steam plumes produced during this period were found to be lithic rock fragments, which is consistent with what is expected from the breaching of a hydrothermal system. The progressive sagging and intrusion of the rock mass into the hydrothermal

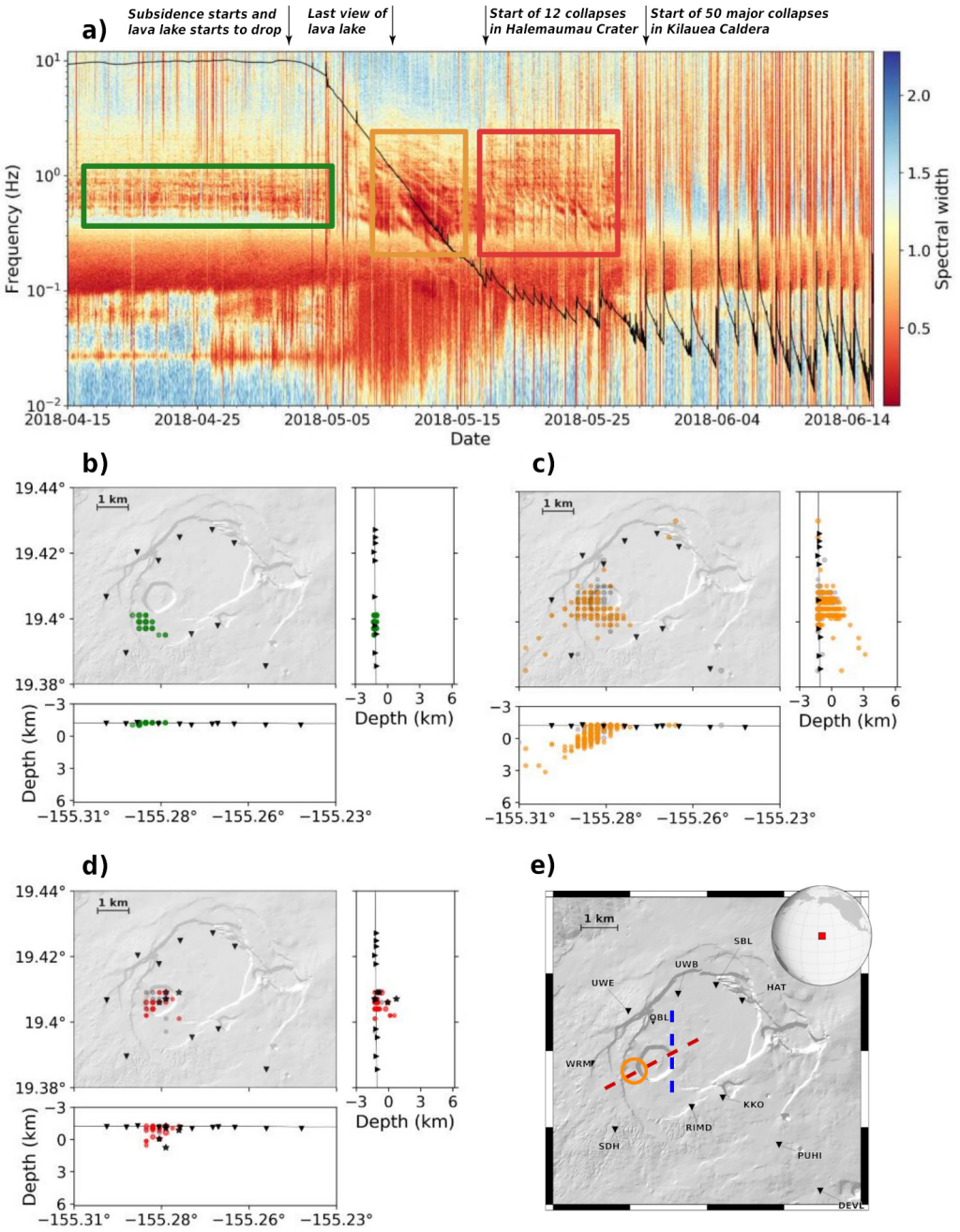

Figure 12: **Application example of shallow tremor characterization at Kilauea, Hawaii**. Modified from Soubestre et al. (2021). (a) Time-frequency-dependent spectral width computed from two months of data recorded by a network composed of 12 broadband seismic stations deployed at the summit of Kilauea. It is computed with the following parameters explained in section 6.3: time windows of length $\Delta_t = 500$ s composed of $M = 10$ subwindows of length $\delta_t = 100$ s overlapping at 50 %. The time series of a tiltmeter co-located with one of the seismometers on the northwest flank of Kilauea Caldera is shown as a black line superimposed on the spectral width plot. Distinct tremor sources can be identified in this figure: long-period tremor before May 5 (green box), first sequence of gliding tremor between May 7 and May 16 (orange box), second sequence of gliding tremor between May 17 and May 27 (red box). Location of tremor sources corresponding to long-period tremor (b), first sequence of gliding tremor (c) and second sequence of gliding tremor (d). (e) Dykes (red and blue dashed lines) and collapse region (orange circle) discussed in the text. Seismic stations appear as black inverted triangles.

reservoir generates swarms of low-amplitude regularly repeating earthquakes modeled by a Dirac comb effect. The spectral gliding characterized by the decrease of frequencies observed in the data corresponds to the decrease of the fundamental frequency and harmonics of the Dirac comb spectrum due to a pro-

gressive increase in the time interval τ between successive earthquakes in the swarms (following Hotovec et al. (2013); Dmitrieva et al. (2013) who observed an opposite gliding trend towards higher frequency associated with accelerating earthquakes):

$$f_n = n/\tau \tag{27}$$

where n stands for the index of fundamental frequency ($n = 1$) and harmonics ($n \geq 2$), and $\tau = \tau_{stick} + \tau_{slip}$ is the stick-slip duration with τ_{stick} and τ_{slip} the duration of an individual downward piston movement and stuck piston, respectively. The stick-slip piston model is applied to two successive swarms with 55.5 hour and 90.5 hour duration, during which the stick-slip duration τ increased from 2.23 s at 11:00 UTC on May 7 to 5.05 s at 05:30 UTC on May 14. Waveforms from individual earthquakes therefore overlap in time and cannot be distinguished in the seismic traces that look like continuous tremor (Hotovec et al., 2013; Dmitrieva et al., 2013). The modeled piston consists of a cylindrical rock mass of 2.07×10^{11} kg with radius of 325 m and height of 250 m progressively intruding 12.3 m through 169,466 small piston strokes into a shallow hydrothermal reservoir with volume of 10^8 m^3 and depth extent of 300 m. The intruded volume represents 4.1 % of the reservoir initial volume (see Soubestre et al. (2021) for more details about the different estimates mentioned in this paragraph).

The second sequence of discrete gliding tremor occurs between May 17 and May 27, when 12 roof collapses took place within Halemaumau Crater (visible as pulses on the tilt signal in Figure 12a). Sources of this gliding tremor are located within the crater (red dots, Figure 12d) and coincide with the position of the 2.9 km $\times$ 2.9 km east-striking dyke imaged by Chouet and Dawson (2011) beneath the Halemaumau Crater (red dashed line, Figure 12e). This gliding tremor is attributed to a change in the physical properties of the underlying east-trending dyke impacted by the collapses, which triggered the dyke resonance. The spectral gliding, which is manifested in a gradual lowering of the resonant frequencies of the dyke, is interpreted as a decrease of the higher-mode frequencies of the resonating dyke associated with a progressive increase in crack stiffness C (Maeda and Kumagai, 2017):

$$f_m = \frac{(m-1)\, v_s}{2L\sqrt{1 + 2\epsilon_m C}} \tag{28}$$

where m represents the mode number, v_s is the sound velocity of the fluid filling the dyke, ϵ_m is a constant dependent on the crack aspect ratio W/L (here equal to 1) and the mode number, and L and W are the crack length and width, respectively. Using the fluid-filled crack model of Chouet (1986), the increasing stiffness is related to a gradual decrease in the gas volume fraction within the bubbly melt filling the dyke. The gas volume fraction decreases from 4.22 % at the time of collapse #1 (04:15 UTC on May 17), to 1.6×10^{-2} % at the time of collapse #10 (02:15 UTC on May 25), with an associated increase in crack stiffness from 6 to 2620 between collapses #1 and #10, respectively. The temporal evolution of the gas volume fraction during the intervals between collapses is further investigated with a model of gas retro-diffusion. Both the fluid-filled crack model and gas retro-diffusion model are consistent with a quasi to totally degassed magma by the end of the sequence of 12 collapses that affected Halemaumau Crater through May 26 (see Soubestre et al. (2021) for more details about the different estimates mentioned in this paragraph).

7.2 Tremor in a transcrustal magmatic system: KVG, Kamchatka, Russia

The Klyuchevskoy Volcanic Group (KVG) located in the Russian Kamchatka peninsula is one of the World's largest and most active clusters of subduction volcanoes. During recent decades, three volcanoes erupted in this region: Klyuchevskoy, Bezymianny, and Tolbachik (Figure 13c). Seismic tomography (e.g. Koulakov et al., 2020) and seismicity (e.g., Levin et al., 2014; Shapiro et al., 2017a) reveal a deep magmatic reservoir located at the crust-mantle boundary and possibly connected to active volcanoes through a rifting zone developed after a recent subduction reconfiguration. This large-scale structure channels fluids and transfer pressure that play an important role in the activity of the KVG volcanoes and generate intense LP seismicity dominated by tremors. To analyse these tremors, we applied the network covariance matrix based method to 45 stations operated in the vicinity of the KVG (Figure 13b) in the framework of the "Klyuchevskoy Investigation - Seismic Structure of an Extraordinary Volcanic System" experiment (KISS) (Shapiro et al., 2017b). We analyzed frequencies between 0.5 and 5 Hz and selected rather long time windows with length $\Delta_t = 1200$ s (by fixing the number of subwindows at $M = 48$ and the subwindow length at $\delta_t = 50$ s, as detailed in section 6.3) to focus on seismic tremors.

Two main periods of reduced spectral width corresponding to intense seismic tremors can be seen in Figure 13a. The first one started in the beginning of December 2015 and did not end with an eruption.

It continued until mid-February 2016 when the activity partially migrated toward Tolbachik. The second episode corresponded to a subsequent activation that led to an eruption in April 2016. We applied a set of network-based criteria described in detail in Journeau et al. (2022) and selected 13,027 windows identified as tremors or swarms of LP earthquakes and located their sources. Their spatial and temporal distribution is shown in Figures 13b-f.

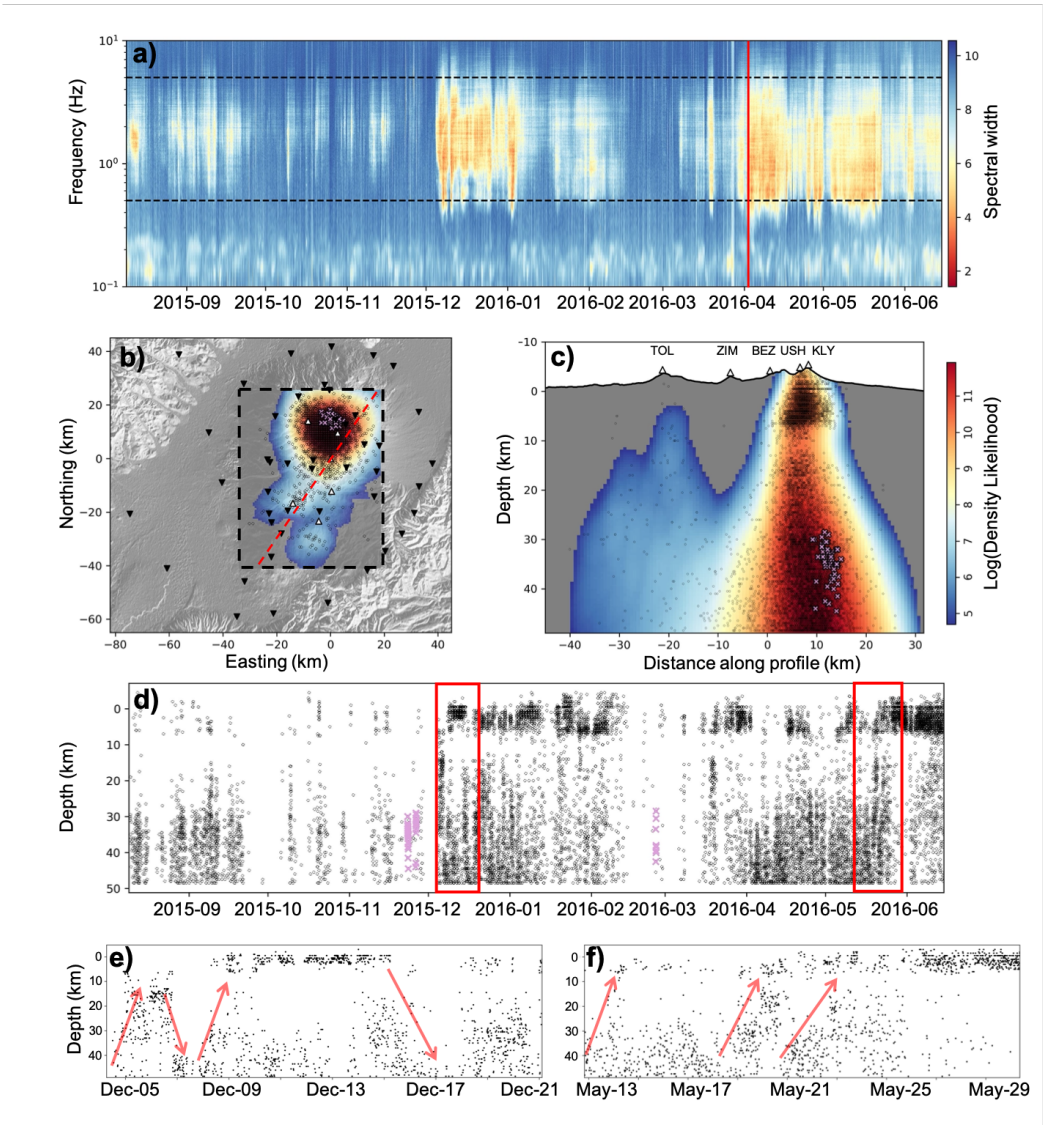

Figure 13: **Application example of tremors analysis within a transcrustal magmatic system, KVG, Kamchatka, Russia**. Modified from Journeau et al. (2022). (a) Covariance matrix spectral width (20) computed for every frequency in 1200 sec long overlapping windows. The two horizontal dashed black lines indicate the frequency band where most of KVG volcanic tremors are observed: 0.5-5 Hz. Red vertical line shows the onset of the Klyuchevskoy eruption on 2016-04-06. (b)-(c) Spatial density of the tremor sources with tremor hypocenters represented as black open circles. (b) Sum along vertical lines projected on the horizontal plane. Seismic stations are shown with black inverted triangles and volcanoes with white triangles. Black dashed rectangle indicates limits of the area used in the grid search. (c) Sum along horizontal lines with fixed depths and along-profile distances projected on a vertical plane corresponding to the profile shown in (b) as a red dashed line. (d) Tremor depth as function of time. Light magenta crosses in (b)-(d) show the DLP swarms that occurred on 23 November 2015, 26 November 2015, and 25 February 2016. (e) and (f) Detailed view on depth-time tremor patterns during periods indicated with red rectangles in (d). Red arrows represent visually identified upward and downward migration episodes.

The network-based location method described in section (6.7) results in a spatial likelihood function

(e.g., Figure 11) computed on a 3-D grid covering the 55 km × 70 km region shown by a black-dashed rectangle in Figure 13b down to 50 km depth, with a 650 m horizontal resolution and a 500 m vertical resolution. To characterize the overall spatial distribution of the tremor sources, we stacked all these likelihood functions. The result shown in Figures 13b-c delineates the active parts of the plumbing system. The highest source density is observed beneath the main part of the KVG including Klyuchevskoy, Bezymianny, and Ushkovsky. A smaller number of sources are located beneath Tolbachik and Udina. This suggests that the active plumbing system extends approximately 50 km along the rift structure (Koulakov et al., 2020) from southwest of Tolbachik volcano to north-east of Klyuchevskoy volcano. The vertical cross-section (Figure 13c) shows that the active plumbing system extends through the whole crust, with the Moho-level magmatic reservoir being connected to Klyuchevskoy via a main conduit and to Tolbachik Udina volcano via a branch deviating at ∼25 km depth.

The space-time distribution of the tremor hypocenters (Figures 13d-f) is not fully random and is mainly composed of short bursts. A detailed view of these bursts reveals migration-like patterns when the activity moves very rapidly from depth toward the surface. We visually identified different upward and downward migration episodes and approximately represented them with simple linear trends (red arrows in Figures 13e-f). The resulting migration velocities were approximately estimated between 3 and 10 km/hour (Journeau et al., 2022). While, most of the time, the tremor activity occurs approximately beneath the Klyuchevskoy volcano, during a few episodes it migrates laterally toward Tolbachik.

The observed spatio-temporal patterns of tremor sources constrain the physical mechanisms controlling the evolution of the activity. Rapid migrations (red arrows, Figures 13e-f) are unlikely to be explained by magma motion through dykes, because the observed migration speeds (up to 10 km/hour) are faster than those associated with dyke propagation or other volcanic fluid migrations that have been reported to be smaller than 1 km/hour in most of the cases. More importantly, observed downward migrations could not be explained by dyke propagation. These migration patterns are not perfectly aligned and have similarity with random diffusions that may be related to the physics of pressure transfer in a system of hydraulically connected magmatic conduits. Such mechanism has been previously evoked by Shapiro et al. (2017a) to explain the link between DLP and shallow LP earthquakes observed at the KVG, when the activity migrated over ∼ 30 km from the Moho level up to the crust during a few months. This average migration rate of ∼ 1 km/day corresponds to an average conduit diffusivity of $\sim 100 m^2 s^{-1}$. The much faster migration of tremor sources (up to 10 km/hour) reported by Journeau et al. (2022) can arise on top of slower diffusion processes as "pressure waves" in a system with pressure-dependent permeability (Rice, 1992).

Fluid pressure transport with a variable permeability can be modeled as a conduit with multiple low permeability barriers that act as valves (e.g., Honda and Yomogida, 1993; Shapiro et al., 2018) that open and close under certain thresholds. Such behavior can result from the long and heterogeneous process of formation of the trans-crustal volcano-plumbing systems that are built by multiple episodes of magmatic intrusions and remobilizations (e.g., Annen et al., 2005; Cashman et al., 2017), resulting in a strong compositional and mechanical heterogeneity where transport properties are likely to be highly variable in both space and time. In such a system, the overall permeability is proportional to the number of open versus closed valves, which, on average, increases with overall pressure gradient across the system. Closely located valves can interact, which results in cascades forming very rapidly migrating pressure transients (analogous to nonlinear pressure waves) able to propagate in both upward and downward directions (Farge et al., 2021), similar to what we observe for the KVG tremors. The modeling shows that in a conduit with background diffusivity of $\sim 100 m^2 s^{-1}$, the cascades of opening and closing valves can migrate with velocities up to ∼ 10 km/hour, which is close to the observations presented here.

This example from KVG shows that analysis of tremors based on seismic networks with appropriate coverage and density can be used to delineate the active parts of volcano-plumbing systems and to follow their hydrodynamic evolution in time. Note that the accuracy and resolution of the tremor spatial likelihood is limited by the knowledge of the wave propagation speed in the medium and the number of sensors forming the seismic network used in the analysis. In addition, the aperture of the network must be wide enough to allow imaging of the deepest parts of the system.

8 Some conclusive remarks and perspectives

In this chapter, we argued in favor of analysing seismo-volcanic tremors with network-based methods and we described a general framework for such methods based on the network covariance matrix introduced in section 6.1. Such analyzes have many advantages compared to single-station methods, because they result in much better characterisation of properties of tremor wavefields and sources and, in particular, of their

locations. In the past, the network-based analysis could be considered as too heavy and sophisticated for a routine application in volcano observatories. Also, many observatories could operate only relatively small numbers of seismometers. But this situation is rapidly changing with the development of modern instrumentation and of information and communication technologies, making the application of network-based methods much more "affordable". So far, such key steps of the analysis including the estimation of the network covariance matrix and its eigenvalue-eigenvector decomposition (section 6.1), the calculation of the spectral width for the tremor detection (section 6.5), and the analysis of the eigenvectors for the tremor source location (section 6.7) are today available as parts of the open-source Python library CovSeisNet (*https://covseisnet.gricad-pages.univ-grenoble-alpes.fr/covseisnet*). Running this analysis for a network composed of a few tens of seismometers does not require extensive computing ressources, implying that it can be done in nearly real time in many modern volcano observatories.

Methods of the network-based analysis of seismic tremors will continue to be developed and improved. Among many possible directions for this, we can suggest a combination of network-based and polarization analyses. This implies to compute and to analyze covariances between all possible components at all stations of a network. Analysis of tremors excited by simultaneously acting sources should be further pursued. This would require to analyze in more details the eigenvalues and eigenvectors of the network covariance matrix. So far, we presented in sections 6.6 and 6.7 the analysis based on a single dominant eigenvector. This implicitly assumes a single dominant tremor source. In the case of multiple sources, this might be necessary to analyze more than one eigenvector and to use them together with their respective eigenvalues in order to separate different sources.

Another very important direction is combining the network-based analysis with ML. Up to present, most of attempts to apply ML algorithms to seismo-volcanic tremors have been based on single-station records or in combining "single-station" based signal features from a few seismometers. The example shown here in section 6.6 illustrates how different signals/sources can be clustered based directly on a "network-based" representation of the wavefield (the dominant eigenvector of the network covariance matrix has been used in this case). Considering the very strong sensitivity of the inter-station cross-correlations to the properties of the tremor sources (section 5), further developing fully network-based ML approaches might be very interesting.

In this chapter mostly aimed at describing the seismological analysis, we did not provided a detailed review of various physical models that have been suggested to explain the origin of seismic tremors. At the same time, in the two examples shown at the end of the chapter, we tried to illustrate how the network-based analysis can be used to measure properties of the tremors such as time variable spectral content or spatial source location. Those can, in turn, be used to test the hypotheses about the physical origin of tremors. The same two examples illustrate the complexity of the seismo-volcanic tremors that is related to the complex behavior of volcanic systems prior to or during eruptions. This aspect is very important to emphasize to avoid simplifying tremors just as a class (or a set of classes) of signals and to be cautious with their simplistic empirical interpretations. Instead, the tremors should be considered as a seismic manifestation of a non-stationary unfolding of several simultaneous and possibly interacting processes occurring within volcanoes. The final goal of the tremor analysis is to make inferences about these processes. To advance in this direction, many different tremor episodes should be analyzed in possible details and inter-compared. The network-based methods will be one of the key tools for such extended analysis of tremors.

Acknowledgments The development of some methods and research results presented in this chapter was supported by the European Research Council (ERC) under the European Union Horizon 2020 Research and Innovation Programme (grant agreement 787399-SEISMAZE). J. Soubestre benefited from the IS-Tremor project provided by Icelandic Research Fund, Rannis (https://www.rannis.is/) (contract number 217738-051).

References

Aki, K., Fehler, M., and Das, S. (1977). Source mechanism of volcanic tremor: Fluid-driven crack models and their application to the 1963 Kilauea eruption. *Journal of volcanology and geothermal research*, 2(3):259–287.

Aki, K. and Ferrazzini, V. (2000). Seismic monitoring and modeling of an active volcano for prediction. *Journal of Geophysical Research: Solid Earth*, 105(B7):16617–16640.

Aki, K. and Koyanagi, R. (1981). Deep volcanic tremor and magma ascent mechanism under Kilauea, Hawaii. *Journal of Geophysical Research: Solid Earth*, 86(B8):7095–7109.

Almendros, J., Abella, R., Mora, M. M., and Lesage, P. (2014). Array analysis of the seismic wavefield of long-period events and volcanic tremor at Arenal volcano, Costa Rica. *Journal of Geophysical Research: Solid Earth*, 119(7):5536–5559.

Almendros, J., Chouet, B., and Dawson, P. (2001). Spatial extent of a hydrothermal system at Kilauea Volcano, Hawaii, determined from array analyses of shallow long-period seismicity: 1. Method. *Journal of Geophysical Research: Solid Earth*, 106(B7):13565–13580.

Almendros, J., Ibáñez, J., Alguacil, G., Del Pezzo, E., and Ortiz, R. (1997). Array tracking of the volcanic tremor source at Deception Island, Antarctica. *Geophysical Research Letters*, 24(23):3069–3072.

Almendros, J., Ibáñez, J. M., Alguacil, G., and Del Pezzo, E. (1999). Array analysis using circular-wave-front geometry:an application to locate the nearby seismo-volcanic source. *Geophysical Journal International*, 136(1):159–170.

Anderson, K. R., Johanson, I. A., Patrick, M. R., Gu, M., Segall, P., Poland, M. P., Montgomery-Brown, E. K., and Miklius, A. (2019). Magma reservoir failure and the onset of caldera collapse at Kilauea Volcano in 2018. *Science*, 366(6470).

Annen, C., Blundy, J. D., and Sparks, R. S. J. (2005). The Genesis of Intermediate and Silicic Magmas in Deep Crustal Hot Zones. *Journal of Petrology*, 47(3):505–539.

Baggeroer, A. B., Kuperman, W. A., and Schmidt, H. (1988). Matched field processing: Source localization in correlated noise as an optimum parameter estimation problem. *The Journal of the Acoustical Society of America*, 83(2):571–587.

Ballmer, S., Wolfe, C. J., Okubo, P. G., Haney, M. M., and Thurber, C. H. (2013). Ambient seismic noise interferometry in Hawai'i reveals long-range observability of volcanic tremor. *Geophysical Journal International*, 194(1):512–523.

Barajas, A., Journeau, C., Obara, K., and Shapiro, N. M. (2023). Comparison of continuously recorded seismic wavefields in tectonic and volcanic environments based on the network covariance matrix. *Journal of Geophysical Research: Solid Earth*, (in revision).

Battaglia, J. and Aki, K. (2003). Location of seismic events and eruptive fissures on the Piton de la Fournaise volcano using seismic amplitudes. *Journal of Geophysical Research: Solid Earth*, 108(B8).

Battaglia, J., Aki, K., and Ferrazzini, V. (2005a). Location of tremor sources and estimation of lava output using tremor source amplitude on the Piton de la Fournaise volcano: 1. Location of tremor sources. *Journal of volcanology and geothermal research*, 147(3-4):268–290.

Battaglia, J., Aki, K., and Staudacher, T. (2005b). Location of tremor sources and estimation of lava output using tremor source amplitude on the Piton de la Fournaise volcano: 2. Estimation of lava output. *Journal of Volcanology and Geothermal Research*, 147(3):291–308.

Battaglia, J., Brenguier, F., and Roult, G. (2016). *Seismic Monitoring at Piton de la Fournaise*, pages 223–242. Springer Berlin Heidelberg, Berlin, Heidelberg.

Bean, C. J., De Barros, L., Lokmer, I., Métaxian, J.-P., O'Brien, G., and Murphy, S. (2014). Long-period seismicity in the shallow volcanic edifice formed from slow-rupture earthquakes. *Nature Geoscience*, 7(1):71–75.

Bensen, G. D., Ritzwoller, M. H., Barmin, M. P., Levshin, a. L., Lin, F., Moschetti, M. P., Shapiro, N. M., and Yang, Y. (2007). Processing seismic ambient noise data to obtain reliable broad-band surface wave dispersion measurements. *Geophys. J. Int.*, 169(3):1239–1260.

Burtin, A., Cattin, R., Bollinger, L., Vergne, J., Steer, P., Robert, A., Findling, N., and Tiberi, C. (2011). Towards the hydrologic and bed load monitoring from high-frequency seismic noise in a braided river: The "torrent de St Pierre", French Alps. *Journal of Hydrology*, 408(1):43–53.

Campillo, M. and Margerin, L. (2010). *Mesoscopic Seismic Waves*, page 188–205. Cambridge University Press.

Cannata, A., Di Grazia, G., Aliotta, M., Cassisi, C., Montalto, P., and Patanè, D. (2013). Monitoring seismo-volcanic and infrasonic signals at volcanoes: Mt. Etna case study. *Pure and Applied Geophysics*, 170(11):1751–1771.

Cannata, A., Di Grazia, G., Montalto, P., Ferrari, F., Nunnari, G., Patanè, D., and Privitera, E. (2010). New insights into banded tremor from the 2008–2009 Mount Etna eruption. *Journal of Geophysical Research: Solid Earth*, 115(B12).

Carbone, D., Zuccarello, L., and Saccorotti, G. (2008). Geophysical indications of magma uprising at Mt Etna during the December 2005 to January 2006 non-eruptive period. *Geophysical Research Letters*, 35(6).

Cashman, K. V., Sparks, R. S. J., and Blundy, J. D. (2017). Vertically extensive and unstable magmatic systems: A unified view of igneous processes. *Science*, 355(6331).

Caudron, C., Girona, T., Jolly, A., Christenson, B., Savage, M. K., Carniel, R., Lecocq, T., Kennedy, B., Lokmer, I., Yates, A., et al. (2021). A quest for unrest in multiparameter observations at Whakaari/White Island volcano, New Zealand 2007–2018. *Earth, Planets and Space*, 73(1):1–21.

Caudron, C., Soubestre, J., Lecocq, T., White, R. S., Brandsdóttir, B., and Krischer, L. (2022). Insights into the dynamics of the 2010 Eyjafjallajökull eruption using seismic interferometry and network covariance matrix analyses. *Earth and Planetary Science Letters*, 585:117502.

Caudron, C., Taisne, B., Kugaenko, Y., and Saltykov, V. (2015). Magma migration at the onset of the 2012–13 Tolbachik eruption revealed by Seismic Amplitude Ratio Analysis. *Journal of Volcanology and Geothermal Research*, 307:60–67.

Caudron, C., White, R. S., Green, R. G., Woods, J., Ágústsdóttir, T., Donaldson, C., Greenfield, T., Rivalta, E., and Brandsdóttir, B. (2018). Seismic Amplitude Ratio Analysis of the 2014–2015 Bárdarbunga-Holuhraun dike propagation and eruption. *Journal of Geophysical Research: Solid Earth*, 123(1):264–276.

Chouet, B. (1986). Dynamics of a fluid-driven crack in three dimensions by the finite difference method. *Journal of Geophysical Research: Solid Earth*, 91(B14):13967–13992.

Chouet, B. (2003). Volcano seismology. *Pure and applied geophysics*, 160(3):739–788.

Chouet, B. and Dawson, P. (2011). Shallow conduit system at Kilauea Volcano, Hawaii, revealed by seismic signals associated with degassing bursts. *Journal of Geophysical Research: Solid Earth*, 116(B12).

Chouet, B., Dawson, P., James, M. R., and Lane, S. J. (2010). Seismic source mechanism of degassing bursts at Kilauea Volcano, Hawaii: Results from waveform inversion in the 10–50 s band. *Journal of Geophysical Research: Solid Earth*, 115(B9).

Chouet, B., De Luca, G., Milana, G., Dawson, P., Martini, M., and Scarpa, R. (1998). Shallow velocity structure of Stromboli Volcano, Italy, derived from small-aperture array measurements of Strombolian tremor. *Bulletin of the Seismological Society of America*, 88(3):653–666.

Chouet, B., Saccorotti, G., Dawson, P., Martini, M., Scarpa, R., De Luca, G., Milana, G., and Cattaneo, M. (1999). Broadband measurements of the sources of explosions at Stromboli Volcano, Italy. *Geophysical research letters*, 26(13):1937–1940.

Chouet, B., Saccorotti, G., Martini, M., Dawson, P., De Luca, G., Milana, G., and Scarpa, R. (1997). Source and path effects in the wave fields of tremor and explosions at Stromboli Volcano, Italy. *Journal of Geophysical Research: Solid Earth*, 102(B7):15129–15150.

Chouet, B. A. (1996). Long-period volcano seismicity: its source and use in eruption forecasting. *Nature*, 380(6572):309–316.

Chouet, B. A. and Matoza, R. S. (2013). A multi-decadal view of seismic methods for detecting precursors of magma movement and eruption. *Journal of Volcanology and Geothermal Research*, 252:108–175.

Cortés, G., Carniel, R., Lesage, P., Mendoza, M. Á., and Della Lucia, I. (2021). Practical volcano-independent recognition of seismic events: Vulcan.ears project. *Frontiers in Earth Science*, 8.

Dawson, P. and Chouet, B. (2014). Characterization of very-long-period seismicity accompanying summit activity at Kilauea Volcano, Hawai'i: 2007–2013. *Journal of Volcanology and Geothermal Research*, 278:59–85.

Di Grazia, G., Falsaperla, S., and Langer, H. (2006). Volcanic tremor location during the 2004 Mount Etna lava effusion. *Geophysical research letters*, 33(4).

Di Lieto, B., Saccorotti, G., Zuccarello, L., Rocca, M. L., and Scarpa, R. (2007). Continuous tracking of volcanic tremor at Mount Etna, Italy. *Geophysical Journal International*, 169(2):699–705.

Dmitrieva, K., Hotovec-Ellis, A. J., Prejean, S., and Dunham, E. M. (2013). Frictional-faulting model for harmonic tremor before Redoubt Volcano eruptions. *Nature Geoscience*, 6(8):652–656.

Droznin, D., Shapiro, N., Droznina, S. Y., Senyukov, S., Chebrov, V., and Gordeev, E. (2015). Detecting and locating volcanic tremors on the Klyuchevskoy group of volcanoes (Kamchatka) based on correlations of continuous seismic records. *Geophysical Journal International*, 203(2):1001–1010.

Dumont, Q., Cayol, V., and Froger, J.-L. (2021). Mitigating bias in inversion of InSAR data resulting from radar viewing geometries. *Geophysical Journal International*, 227(1):483–495.

Duputel, Z., Ferrazzini, V., Lengliné, O., Michon, L., Fontaine, F. R., and Massin, F. (2021). Seismicity of La Réunion island. *Comptes Rendus. Géoscience*, 353(S1):237–255.

Eibl, E. P., Bean, C. J., Einarsson, B., Pàlsson, F., and Vogfjörd, K. S. (2020). Seismic ground vibrations give advanced early-warning of subglacial floods. *Nature communications*, 11(1):1–11.

Eibl, E. P., Bean, C. J., Jónsdóttir, I., Höskuldsson, A., Thordarson, T., Coppola, D., Witt, T., and Walter, T. R. (2017a). Multiple coincident eruptive seismic tremor sources during the 2014–2015 eruption at Holuhraun, Iceland. *Journal of Geophysical Research: Solid Earth*, 122(4):2972–2987.

Eibl, E. P., Bean, C. J., Vogfjörd, K. S., Ying, Y., Lokmer, I., Möllhoff, M., O'Brien, G. S., and Pálsson, F. (2017b). Tremor-rich shallow dyke formation followed by silent magma flow at Bárdarbunga in Iceland. *Nature Geoscience*, 10(4):299–304.

Eibl, E. P. S., Thordarson, T., Höskuldsson, , Gudnason, E. , Dietrich, T., Hersir, G. P., and Ágústsdóttir, T. (2023). Evolving shallow conduit revealed by tremor and vent activity observations during episodic lava fountaining of the 2021 geldingadalir eruption, iceland. *Bulletin of Volcanology*, 85.

Endo, E. T. and Murray, T. (1991). Real-time seismic amplitude measurement (RSAM): a volcano monitoring and prediction tool. *Bulletin of Volcanology*, 53(7):533–545.

Ereditato, D. and Luongo, G. (1994). Volcanic tremor wave field during quiescent and eruptive activity at Mt. Etna (Sicily). *Journal of volcanology and geothermal research*, 61(3-4):239–251.

Farge, G., Jaupart, C., and Shapiro, N. M. (2021). Episodicity and migration of low frequency earthquakes modeled with fast fluid pressure transients in the permeable subduction interface. *Journal of Geophysical Research: Solid Earth*, 126(9):e2021JB021894.

Fee, D., Haney, M. M., Matoza, R. S., Eaton, A. R. V., Cervelli, P., Schneider, D. J., and Iezzi, A. M. (2017). Volcanic tremor and plume height hysteresis from Pavlof Volcano, Alaska. *Science*, 355(6320):45–48.

Fehler, M. (1983). Observations of volcanic tremor at Mount St. Helens volcano. *Journal of Geophysical Research: Solid Earth*, 88(B4):3476–3484.

Ferrazzini, V., Aki, K., and Chouet, B. (1991). Characteristics of seismic waves composing Hawaiian volcanic tremor and gas-piston events observed by a near-source array. *Journal of Geophysical Research: Solid Earth*, 96(B4):6199–6209.

Fujita, E. (2008). Banded tremor at Miyakejima volcano, Japan: Implication for two-phase flow instability. *Journal of Geophysical Research: Solid Earth*, 113(B4).

Furumoto, M., Kunitomo, T., Inoue, H., Yamada, I., Yamaoka, K., Ikami, A., and Fukao, Y. (1990). Twin sources of high-frequency volcanic tremor of Izu-Oshima Volcano, Japan. *Geophysical Research Letters*, 17(1):25–27.

Furumoto, M., Kunitomo, T., Inoue, H., and Yamaoka, K. (1992). Seismic image of the volcanic tremor source at Izu-Oshima volcano, Japan. In *Volcanic Seismology*, pages 201–211. Springer.

Gerstoft, P., Menon, R., Hodgkiss, W. S., and Mecklenbräuker, C. F. (2012). Eigenvalues of the sample covariance matrix for a towed array. *The Journal of the Acoustical Society of America*, 132(4):2388–2396.

Gimbert, F., Tsai, V. C., and Lamb, M. P. (2014). A physical model for seismic noise generation by turbulent flow in rivers. *Journal of Geophysical Research: Earth Surface*, 119(10):2209–2238.

Girona, T., Caudron, C., and Huber, C. (2019). Origin of shallow volcanic tremor: The dynamics of gas pockets trapped beneath thin permeable media. *Journal of Geophysical Research: Solid Earth*, 124(5):4831–4861.

Goldstein, P. and Chouet, B. (1994). Array measurements and modeling of sources of shallow volcanic tremor at Kilauea Volcano, Hawaii. *Journal of Geophysical Research: Solid Earth*, 99(B2):2637–2652.

Gordeev, E. I., Saltykov, V. A., Sinitsyn, V. I., and Chebrov, V. N. (1990). Temporal and spatial characteristics of volcanic tremor wave fields. *Journal of Volcanology and Geothermal Research*, 40(1):89–101.

Gottschämmer, E. and Surono, I. (2000). Locating tremor and shock sources recorded at Bromo Volcano. *Journal of volcanology and geothermal research*, 101(1-2):199–209.

Gudmundsson, M. T., Pedersen, R., Vogfjörd, K., Thorbjarnardóttir, B., Jakobsdóttir, S., and Roberts, M. J. (2010). Eruptions of Eyjafjallajökull Volcano, Iceland. *Eos, Transactions American Geophysical Union*, 91(21):190–191.

Gudmundsson, Ó. and Brandsdóttir, B. (2010). Geothermal noise at ölkelduháls, SW Iceland. *Jökull*, 60:89–102.

Haney, M. M., Fee, D., McKee, K. F., Lyons, J. J., Matoza, R. S., Wech, A. G., Tepp, G., Searcy, C., and Mikesell, T. D. (2020). Co-eruptive tremor from Bogoslof volcano: seismic wavefield composition at regional distances. *Bulletin of Volcanology*, 82(2):1–14.

Honda, S. and Yomogida, K. (1993). Periodic magma movement in the conduit with a barrier: A model for the volcanic tremor. *Geophysical Research Letters*, 20(3):229–232.

Hotovec, A. J., Prejean, S. G., Vidale, J. E., and Gomberg, J. (2013). Strongly gliding harmonic tremor during the 2009 eruption of Redoubt Volcano. *Journal of Volcanology and Geothermal Research*, 259:89–99.

Ichihara, M. (2016). Seismic and infrasonic eruption tremors and their relation to magma discharge rate: A case study for sub-Plinian events in the 2011 eruption of Shinmoe-dake, Japan. *Journal of Geophysical Research: Solid Earth*, 121(10):7101–7118.

Ichimura, M., Yokoo, A., Kagiyama, T., Yoshikawa, S., and Inoue, H. (2018). Temporal variation in source location of continuous tremors before ash–gas emissions in january 2014 at Aso volcano, Japan. *Earth, Planets and Space*, 70(1):1–15.

Iverson, R. M., Dzurisin, D., Gardner, C. A., Gerlach, T. M., LaHusen, R. G., Lisowski, M., Major, J. J., Malone, S. D., Messerich, J. A., Moran, S. C., et al. (2006). Dynamics of seismogenic volcanic extrusion at Mount St Helens in 2004–05. *Nature*, 444(7118):439–443.

Jellinek, A. M. and Bercovici, D. (2011). Seismic tremors and magma wagging during explosive volcanism. *Nature*, 470(7335):522–525.

Jones, J., Carniel, R., and Malone, S. (2012). Decomposition, location, and persistence of seismic signals recovered from continuous tremor at Erta'Ale, Ethiopia. *Journal of Volcanology and Geothermal Research*, 213:116–129.

Journeau, C., Shapiro, N. M., Seydoux, L., Soubestre, J., Ferrazzini, V., and Peltier, A. (2020). Detection, classification, and location of seismovolcanic signals with multicomponent seismic data: example from the Piton de La Fournaise Volcano (La Réunion, France). *Journal of Geophysical Research: Solid Earth*, 125(8):e2019JB019333.

Journeau, C., Shapiro, N. M., Seydoux, L., Soubestre, J., Koulakov, I. Y., Jakovlev, A. V., Abkadyrov, I., Gordeev, E. I., Chebrov, D. V., Droznin, D. V., et al. (2022). Seismic tremor reveals active trans-crustal magmatic system beneath Kamchatka volcanoes. *Science advances*, 8(5):eabj1571.

Julian, B. R. (1994). Volcanic tremor: Nonlinear excitation by fluid flow. *Journal of Geophysical Research: Solid Earth*, 99(B6):11859–11877.

Kawakatsu, H., Kaneshima, S., Matsubayashi, H., Ohminato, T., Sudo, Y., Tsutsui, T., Uhira, K., Yamasato, H., Ito, H., and Legrand, D. (2000). Aso94: Aso seismic observation with broadband instruments. *Journal of Volcanology and Geothermal Research*, 101(1-2):129–154.

Kawakatsu, H., Ohminato, T., and Ito, H. (1994). 10s-period volcanic tremors observed over a wide area in southwestern Japan. *Geophysical Research Letters*, 21(18):1963–1966.

Kedar, S., Kanamori, H., and Sturtevant, B. (1998). Bubble collapse as the source of tremor at Old Faithful Geyser. *Journal of Geophysical Research: Solid Earth*, 103(B10):24283–24299.

Kedar, S., Sturtevant, B., and Kanamori, H. (1996). The origin of harmonic tremor at Old Faithful geyser. *Nature*, 379(6567):708–711.

Konstantinou, K. I. and Schlindwein, V. (2002). Nature, wavefield properties and source mechanism of volcanic tremor: a review. *Journal of Volcanology and Geothermal Research*, 119(1-4):161–187.

Koulakov, I., Shapiro, N. M., Sens-Schönfelder, C., Luehr, B. G., Gordeev, E. I., Jakovlev, A., Abkadyrov, I., Chebrov, D. V., Bushenkova, N., Droznina, S. Y., Senyukov, S. L., Novgorodova, A., and Stupina, T. (2020). Mantle and crustal sources of magmatic activity of Klyuchevskoy and surrounding volcanoes in Kamchatka inferred from earthquake tomography. *Journal of Geophysical Research: Solid Earth*, 125(10):e2020JB020097.

Kumagai, H. (2009). *Volcano Seismic Signals, Source Quantification of*, pages 9899–9932. Springer New York, New York, NY.

Kumagai, H., Londoño, J. M., Maeda, Y., and Acevedo Rivas, A. E. (2019). Amplitude source location method with depth-dependent scattering and attenuation structures: Application at Nevado del Ruiz volcano, Colombia. *Journal of Geophysical Research: Solid Earth*, 124(11):11585–11600.

Kumagai, H., Nakano, M., Maeda, T., Yepes, H., Palacios, P., Ruiz, M., Arrais, S., Vaca, M., Molina, I., and Yamashima, T. (2010). Broadband seismic monitoring of active volcanoes using deterministic and stochastic approaches. *Journal of Geophysical Research: Solid Earth*, 115(B8).

Kumagai, H., Ohminato, T., Nakano, M., Ooi, M., Kubo, A., Inoue, H., and Oikawa, J. (2001). Very-long-period seismic signals and caldera formation at Miyake Island, Japan. *Science*, 293(5530):687–690.

Kumagai, H., Palacios, P., Maeda, T., Castillo, D. B., and Nakano, M. (2009). Seismic tracking of lahars using tremor signals. *Journal of Volcanology and Geothermal Research*, 183(1-2):112–121.

Kuperman, W. and Turek, G. (1997). Matched field acoustics. *Mechanical Systems and Signal Processing*, 11(1):141–148.

Lahr, J., Chouet, B., Stephens, C., Power, J., and Page, R. (1994). Earthquake classification, location, and error analysis in a volcanic environment: implications for the magmatic system of the 1989–1990 eruptions at Redoubt Volcano, Alaska. *Journal of Volcanology and Geothermal Research*, 62(1):137–151.

Leet, R. C. (1988). Saturated and subcooled hydrothermal boiling in groundwater flow channels as a source of harmonic tremor. *Journal of Geophysical Research: Solid Earth*, 93(B5):4835–4849.

Levin, V., Droznina, S., Gavrilenko, M., Carr, M. J., and Senyukov, S. (2014). Seismically active sub-crustal magma source of the Klyuchevskoy volcano in Kamchatka, Russia. *Geology*, 42(11):983–986.

Levshin, A. L., Yanovskaya, T. B., Lander, A. V., Bukchin, B. G., Barmin, M. P., Ratnikova, L. I., and Its, E. (1989). *Seismic Surface Waves in a Laterally Inhomogeneous Earth*. Springer, New York.

Li, K. L., Bean, C. J., Bell, A. F., Ruiz, M., Hernandez, S., and Grannell, J. (2022). Seismic tremor reveals slow fracture propagation prior to the 2018 eruption at Sierra Negra volcano, Galápagos. *Earth and Planetary Science Letters*, 586:117533.

Li, K. L. and Gudmundsson, O. (2020). A probabilistic tremor location method. *Geophysical Research Letters*, 47(4):e2019GL085538.

Maeda, Y. and Kumagai, H. (2017). A generalized equation for the resonance frequencies of a fluid-filled crack. *Geophysical Journal International*, 209(1):192–201.

Maggi, A., Ferrazzini, V., Hibert, C., Beauducel, F., Boissier, P., and Amemoutou, A. (2017). Implementation of a multistation approach for automated event classification at Piton de la Fournaise volcano. *Seismological Research Letters*, 88(3):878–891.

Makus, P., Sens-Schönfelder, C., Illien, L., Walter, T. R., Yates, A., and Tilmann, F. (2023). Deciphering the whisper of volcanoes: Monitoring velocity changes at Kamchatka's Klyuchevskoy Group with fluctuating noise fields. *Journal of Geophysical Research: Solid Earth*, page e2022JB025738.

Matoza, R. S. and Chouet, B. A. (2010). Subevents of long-period seismicity: Implications for hydrothermal dynamics during the 2004–2008 eruption of Mount St. Helens. *Journal of Geophysical Research: Solid Earth*, 115(B12).

McNutt, S. R. (1992). Volcanic tremor. *Encyclopedia of earth system science*, 4:417–425.

McNutt, S. R. (1994). Volcanic tremor amplitude correlated with the volcano explosivity index and its potential use in determining ash hazards to aviation. *U.S. Geological Survey Bulletin*, 2047:377–385.

McNutt, S. R. and Nishimura, T. (2008a). Volcanic tremor during eruptions: temporal characteristics, scaling and constraints on conduit size and processes. *Journal of Volcanology and Geothermal Research*, 178(1):10–18.

McNutt, S. R. and Nishimura, T. (2008b). Volcanic tremor during eruptions: Temporal characteristics, scaling and constraints on conduit size and processes. *Journal of Volcanology and Geothermal Research*, 178(1):10–18. Dynamics of Volcanic Explosions: Field Observations, Experimental Constraints and Integrated Modelling of Volcanic Explosions: Field Observations, Experimental Constraints and Integrated Modelling.

Melnik, O., Lyakhovsky, V., Shapiro, N. M., Galina, N., and Bergal-Kuvikas, O. (2020). Deep long period volcanic earthquakes generated by degassing of volatile-rich basaltic magmas. *Nature Communications*, 11(1):3918.

Métaxian, J.-P., Lesage, P., and Valette, B. (2002). Locating sources of volcanic tremor and emergent events by seismic triangulation: Application to Arenal volcano, Costa Rica. *Journal of Geophysical Research: Solid Earth*, 107(B10):ECV–10.

Mori, A., Kumagai, H., and Londoño, J. M. (2022). Plume height, duration and volume of sustained explosive eruptions inferred from eruption tremor amplitudes. *Geophysical Journal International*, 231(2):1045–1056.

Moschella, S., Cannata, A., Di Grazia, G., and Gresta, S. (2018). Insights into lava fountain eruptions at Mt. Etna by improved source location of the volcanic tremor. *Annals of Geophysics*.

Métaxian, J., Lesage, P., and Dorel, J. (1997). Permanent tremor of Masaya Volcano, Nicaragua: Wave field analysis and source location. *Journal of Geophysical Research: Solid Earth*, 102(B10):22529–22545.

Nadeau, R. M. and Dolenc, D. (2005). Nonvolcanic tremors deep beneath the San Andreas fault. *Science*, 307(5708):389–389.

Nanni, U., Gimbert, F., Roux, P., and Lecointre, A. (2021). Observing the subglacial hydrology network and its dynamics with a dense seismic array. *Proceedings of the National Academy of Sciences*, 118(28):e2023757118.

Neal, C., Brantley, S., Antolik, L., Babb, J., Burgess, M., Calles, K., Cappos, M., Chang, J., Conway, S., Desmither, L., et al. (2018). The 2018 rift eruption and summit collapse of Kilauea Volcano. *Science*, page eaav7046.

Newhall, C. G. and Self, S. (1982). The volcanic explosivity index (VEI) an estimate of explosive magnitude for historical volcanism. *Journal of Geophysical Research: Oceans*, 87(C2):1231–1238.

Nishimura, T., Hamaguchi, H., and Ueki, S. (1995). Source mechanisms of volcanic tremor and low-frequency earthquakes associated with the 1988–89 eruptive activity of Mt Tokachi, Hokkaido, Japan. *Geophysical Journal International*, 121(2):444–458.

Nishimura, T., Nakamichi, H., Tanaka, S., Sato, M., Kobayashi, T., Ueki, S., Hamaguchi, H., Ohtake, M., and Sato, H. (2000). Source process of very long period seismic events associated with the 1998 activity of Iwate Volcano, northeastern Japan. *Journal of Geophysical Research: Solid Earth*, 105(B8):19135–19147.

Obara, K. (2002). Nonvolcanic deep tremor associated with subduction in southwest Japan. *Science*, 296(5573):1679–1681.

Ogiso, M., Matsubayashi, H., and Yamamoto, T. (2015). Descent of tremor source locations before the 2014 phreatic eruption of Ontake volcano, Japan. *Earth, Planets and Space*, 67(1):1–12.

Ogiso, M. and Yomogida, K. (2012). Migration of tremor locations before the 2008 eruption of Meakan-dake Volcano, Hokkaido, Japan. *Journal of Volcanology and Geothermal Research*, 217:8–20.

Ogiso, M. and Yomogida, K. (2021). Estimation of relative source locations from seismic amplitude: application to earthquakes and tremors at Meakandake volcano, eastern Hokkaido, Japan. *Earth, Planets and Space*, 73(1):1–14.

Orchard, J., Ebrahimi, M., and Wong, A. (2008). Efficient nonlocal-means denoising using the SVD. In *2008 15th IEEE International Conference on Image Processing*, pages 1732–1735. IEEE.

Patanè, D., Di Grazia, G., Cannata, A., Montalto, P., and Boschi, E. (2008). Shallow magma pathway geometry at Mt. Etna volcano. *Geochemistry, Geophysics, Geosystems*, 9(12).

Permana, T., Nishimura, T., Nakahara, H., Fujita, E., and Ueda, H. (2019). Reliability evaluation of volcanic tremor source location determination using cross-correlation functions. *Geophysical Journal International*, 220(2):1300–1315.

Podolskiy, E. A. and Walter, F. (2016). Cryoseismology. *Reviews of Geophysics*, 54(4):708–758.

Poland, M. P. and Anderson, K. R. (2020). Partly cloudy with a chance of lava flows: Forecasting volcanic eruptions in the twenty-first century. *Journal of Geophysical Research: Solid Earth*, 125(1):e2018JB016974.

Rice, J. R. (1992). Chapter 20 Fault Stress States, Pore Pressure Distributions, and the Weakness of the San Andreas Fault. In Evans, B. and Wong, T.-f., editors, *International Geophysics*, volume 51 of *Fault Mechanics and Transport Properties of Rocks*, pages 475–503. Academic Press.

Rost, S. and Thomas, C. (2002). Array seismology: Methods and applications. *Reviews of geophysics*, 40(3):2–1.

Rowe, C., Aster, R., Kyle, P., Dibble, R., and Schlue, J. (2000). Seismic and acoustic observations at Mount Erebus volcano, Ross island, Antarctica, 1994–1998. *Journal of Volcanology and Geothermal Research*, 101(1-2):105–128.

Ruigrok, E., Gibbons, S., and Wapenaar, K. (2017). Cross-correlation beamforming. *Journal of Seismology*, 21.

Ryall, A. and Ryall, F. (1983). Spasmodic tremor and possible magma injection in Long Valley Caldera, Eastern California. *Science*, 219(4591):1432–1433.

Saccorotti, G., Chouet, B., and Dawson, P. (2003). Shallow-velocity models at the Kilauea Volcano, Hawaii, determined from array analyses of tremor wavefields. *Geophysical Journal International*, 152(3):633–648.

Schweitzer, J., Fyen, J., Mykkeltveit, S., Gibbons, S. J., Pirli, M., Kühn, D., and Kværna, T. (2012). Seismic arrays. In *New manual of seismological observatory practice 2 (NMSOP-2)*, pages 1–80. Deutsches GeoForschungsZentrum GFZ.

Seidl, D., Schick, R., and Riuscetti, M. (1981). Volcanic tremors at Etna: a model for hydraulic origin. *Bulletin volcanologique*, 44(1):43–56.

Senyukov, S., Nuzhdina, I., Droznina, S., Garbuzova, V., Kozhevnikova, T., Sobolevskaya, O., Nazarova, Z., and Bliznetsov, V. (2015). Reprint of "Seismic monitoring of the Plosky Tolbachik eruption in 2012–2013 (Kamchatka Peninsula Russia)". *Journal of Volcanology and Geothermal Research*, 307:47–59.

Seydoux, L., Shapiro, N. M., de Rosny, J., Brenguier, F., and Landès, M. (2016). Detecting seismic activity with a covariance matrix analysis of data recorded on seismic arrays. *Geophysical Journal International*, 204(3):1430–1442.

Shapiro, N., Droznin, D. V., Droznina, S. Y., Senyukov, S. L., Gusev, A. A., and Gordeev, E. I. (2017a). Deep and shallow long-period volcanic seismicity linked by fluid-pressure transfer. *Nature geosciences*.

Shapiro, N., Sens-Schönfelder, C., Lühr, B., Weber, M., Abkadyrov, I., Gordeev, E., Koulakov, I., Jakovlev, A., Kugaenko, Y., and Saltykov, V. (2017b). Understanding Kamchatka's extraordinary volcano cluster. *EOS*, 98:12–17.

Shapiro, N. M., Campillo, M., Kaminski, E., Vilotte, J.-P., and Jaupart, C. (2018). Low-frequency earthquakes and pore pressure transients in subduction zones. *Geophysical Research Letters*, 45(20):11,083–11,094.

Smith, P. J. and Bean, C. J. (2020). Retreat: A real-time tremor analysis tool for seismic arrays, with applications for volcano monitoring. *Frontiers in Earth Science*, 8.

Soubestre, J., Chouet, B., and Dawson, P. (2021). Sources of volcanic tremor associated with the summit caldera collapse during the 2018 east rift eruption of Kīlauea Volcano, Hawai'i. *Journal of Geophysical Research: Solid Earth*, 126(6):e2020JB021572.

Soubestre, J., Seydoux, L., Shapiro, N., De Rosny, J., Droznin, D., Droznina, S. Y., Senyukov, S., and Gordeev, E. (2019). Depth migration of seismovolcanic tremor sources below the Klyuchevskoy volcanic group (Kamchatka) determined from a network-based analysis. *Geophysical Research Letters*, 46(14):8018–8030.

Soubestre, J., Shapiro, N. M., Seydoux, L., de Rosny, J., Droznin, D. V., Droznina, S. Y., Senyukov, S. L., and Gordeev, E. I. (2018). Network-based detection and classification of seismovolcanic tremors: Example from the Klyuchevskoy volcanic group in Kamchatka. *Journal of Geophysical Research: Solid Earth*, 123(1):564–582.

Steinke, B., Jolly, A., Carniel, R., Dempsey, D., and Cronin, S. (2023). Identification of seismo-volcanic regimes at Whakaari/White Island (New Zealand) via systematic tuning of an unsupervised classifier. *Journal of Geophysical Research: Solid Earth*, 128(3):e2022JB026221.

Taisne, B., Brenguier, F., Shapiro, N., and Ferrazzini, V. (2011). Imaging the dynamics of magma propagation using radiated seismic intensity. *Geophysical Research Letters*, 38(4).

Titos, M., Bueno, A., García, L., Benítez, M. C., and Ibañez, J. (2019). Detection and classification of continuous volcano-seismic signals with recurrent neural networks. *IEEE Transactions on Geoscience and Remote Sensing*, 57(4):1936–1948.

Unglert, K. and Jellinek, A. (2017). Feasibility study of spectral pattern recognition reveals distinct classes of volcanic tremor. *Journal of Volcanology and Geothermal Research*, 336:219–244.

Unglert, K., Radić, V., and Jellinek, A. M. (2016). Principal component analysis vs. self-organizing maps combined with hierarchical clustering for pattern recognition in volcano seismic spectra. *Journal of Volcanology and Geothermal Research*, 320:58–74.

Vidale, J. E. (1986). Complex polarization analysis of particle motion. *Bulletin of the Seismological Society of America*, 76(5):1393–1405.

Wassermann, J. (2012). *Volcano Seismology*, pages 1–77. Potsdam : Deutsches GeoForschungsZentrum GFZ.

Yamada, T., Kurokawa, A. K., Terada, A., Kanda, W., Ueda, H., Aoyama, H., Ohkura, T., Ogawa, Y., and Tanada, T. (2021). Locating hydrothermal fluid injection of the 2018 phreatic eruption at Kusatsu-Shirane volcano with volcanic tremor amplitude. *Earth, Planets and Space*, 73(1):1–15.

Yates, A., Caudron, C., Lesage, P., Mordret, A., Lecocq, T., and Soubestre, J. (2023). Assessing similarity in continuous seismic cross-correlation functions using hierarchical clustering: application to Ruapehu and Piton de la Fournaise volcanoes. *Geophysical Journal International*, 233(1):472–489.

Zobin, V. M. (2011). *Introduction to Volcanic Seismology*. Elsevier.